

Banner appropriate to article type will appear here in typeset article

Direct numerical simulation of turbulent pipe flow up to $Re_\tau \approx 5200$

Jie Yao¹, Saleh Rezaeiravesh², Philipp Schlatter² and Fazle Hussain¹,

¹Department of Mechanical Engineering, Texas Tech University, Lubbock, Texas, USA, 79409

²Department of Engineering Mechanics, KTH Royal Institute of Technology, SE-100 44 Stockholm, Sweden

(Received xx; revised xx; accepted xx)

Well-resolved direct numerical simulations (DNSs) have been performed of the flow in a smooth circular pipe of radius R and axial length $10\pi R$ at friction Reynolds numbers up to $Re_\tau = 5200$ using the pseudospectral code OPENPIPEFLOW. Various turbulence statistics are documented and compared with other DNS and experimental data in pipes as well as channels. Small but distinct differences between various datasets are identified. The friction factor λ overshoots by 2% and undershoots by 0.6% of the Prandtl friction law at low and high Re ranges, respectively. In addition, λ in our results is slightly higher than that in Pirozzoli *et al.* (Pirozzoli *et al.*, *J. Fluid. Mech.*, 926, A28, 2021), but matches well with the experiments in Furuichi *et al.* (Furuichi *et al.*, *Phys. Fluids*, 27, 095108, 2015). The log-law indicator function, which is nearly indistinguishable between the pipe and channel flows up to $y^+ = 250$, has not yet developed a plateau further away from the wall in the pipes even for the $Re_\tau = 5200$ cases. The wall shear stress fluctuations and the inner peak of the axial velocity intensity – which grow monotonically with Re_τ – are lower in the pipe than in the channel, but the difference decreases with increasing Re_τ . While the wall values are slightly lower in channel than pipe flows at the same Re_τ , the inner peaks of the pressure fluctuations show negligible differences between them. The Reynolds number scaling of all these quantities agrees with both the logarithmic and defect power laws if the coefficients are properly chosen. The one-dimensional spectrum of the axial velocity fluctuation exhibits a k^{-1} dependence at an intermediate distance from the wall – as also seen in the channel flow. In summary, this high-fidelity data enable us to provide better insights into the flow physics in the pipes as well as the similarity/difference among different types of wall turbulence.

1. Introduction

Turbulent flows that are constrained by a wall (referred to as “wall turbulence”) are common in nature and engineering applications. Roughly half of the energy spent in transporting fluids through pipes or vehicles through air or water is dissipated by the turbulence near the walls (Jiménez 2012). Therefore, an improved understanding of the underlying physics of these flows is essential for modeling and control (Kim 2011; Canton *et al.* 2016; Yao *et al.* 2018). The spatially evolving boundary layer, the (plane) channel, and the pipe are three canonical geometrical configurations of wall turbulence. Different from boundary layer and channel flows, azimuthal periodicity is inherent to pipe flows. Therefore, pipe flow is the most canonical case, being completely described by the Reynolds number (Re) and the axial length – the effect of the latter is limited if sufficiently large (El Khoury *et al.* 2013; Feldmann *et al.* 2018).

The sustained interest in high- Re wall turbulence stems from numerous open questions regarding the scaling of turbulent statistics, as reviewed in Marusic *et al.* (2010b) and Smits *et al.* (2011b). For example, a characteristic of high- Re wall turbulence is the logarithmic law in the mean velocity with an important parameter, i.e. the von Kármán constant κ , whose value and universality among different flow geometries are still highly debated (Nagib & Chauhan 2008; She *et al.* 2017). Also, no conclusion has been reached on whether the near-wall peak of the streamwise velocity fluctuations continuously increases with Re (Marusic

et al. 2017) or eventually saturates at high Re (Chen & Sreenivasan 2021; Klewicki 2022). Furthermore, the existence of an outer peak in the streamwise velocity fluctuations, as indicated by experiments, is also highly debated (Hultmark *et al.* 2012; Willert *et al.* 2017). Other questions, which can be answered only with substantially higher Re 's, are the scaling and generation mechanism of the various flow structures. Large-scale (LSMs) and very large-scale motions (VLSMs), with lengths of $5R$ up to $20R$ have been experimentally found in the outer region of pipe flows (Kim & Adrian 1999; Monty *et al.* 2007). Here, R is the radius of the pipe. Due to the increasing strength of these structures with Re , they even leave their footprint quite close to the wall (Monty *et al.* 2007), in the form of amplitude modulation as reviewed by e.g. Dogan *et al.* (2018).

Fundamental studies of wall turbulence require accurate representations or measurements of the flows, which were typically carried out via experiments (Zagarola & Smits 1998; McKeon *et al.* 2005; Smits *et al.* 2011a; Furuichi *et al.* 2015, 2018; Talamelli *et al.* 2009; Fiorini 2017). However, decades of experimental research have shown that obtaining unambiguous high- Re data, particularly near the wall, remains a challenge. That is because as Re increases, the smallest scale decrease – leading to large uncertainties in determining the probe locations and turbulence intensities. Advances in computer technology (both in hardware and software) have enshrined direct numerical simulation (DNS) as an essential tool for turbulence research. Although only moderate Re can be achieved at the current stage, DNS provides extensive, detailed data compared to experiments – even close to the walls where experimental data is very difficult to be obtained. One of the earliest DNS for wall turbulence was performed by Kim *et al.* (1987) for the channel flow at friction Reynolds number $Re_\tau (\equiv u_\tau h/\nu) \approx 180$ (here, u_τ is the friction velocity, h is the half channel height, and ν is the fluid kinematic viscosity). They found good agreements between DNS and experimental data by Hussain & Reynolds (1975), except in the near-wall region. The discrepancy was speculated to be caused by the inherent near-wall turbulence measurement errors. Eggels *et al.* (1994) subsequently conducted the first DNS of pipe flow at $Re_\tau (\equiv u_\tau R/\nu) \approx 180$ to investigate the differences between channel and pipe flows.

Numerous DNS investigations have been carried out in the aftermath of these pioneering studies, with Re progressively increasing as a result of increased computational power (Moser *et al.* 1999; Bernardini *et al.* 2014; Wu & Moin 2008). However, among them, only those with $Re_\tau \geq 10^3$ are of particular engineering interest as this is the range of Re relevant to industrial applications. In addition, it is in this range that the high- Re characteristics of wall turbulence start to manifest. One of the highest Re_τ large domain DNS was performed by Lee & Moser (2015) for channel flows at $Re_\tau = 5186$ with the domain size $L_x \times L_z = 8\pi h \times 3\pi h$. Compared to numerous DNS for channel flows (Lozano-Durán & Jiménez 2014; Bernardini *et al.* 2014; Lee & Moser 2015), fewer high- Re studies have been performed for pipe flow; and most of them are limited to $Re_\tau \approx 1000$. For example, Lee & Sung (2013) performed DNS at $Re_\tau \approx 1000$ with a length of $30R$ and established the existence of VLSM of scale up to $\mathcal{O}(20R)$. El Khoury *et al.* (2013) used a spectral-element method to perform DNS for Re_τ up to 1000 with the length $L_z = 25R$. Chin *et al.* (2014) found that the mean velocity profile does not exhibit a strictly logarithmic layer with Re_τ up to 2000, necessitating a finite- Re correction like those introduced by Afzal (1976) and Jiménez & Moser (2007). To quantify the effects of computational length and Re , Feldmann *et al.* (2018) conducted DNS for $90 \leq Re_\tau \leq 1500$ with L_z up to $42R$. They confirmed that $L_z = 42R$ is sufficiently large to capture the LSM and VLSM-relevant scales. Ahn *et al.* (2015) performed DNS of pipe flow at $Re_\tau \approx 3000$ for a length of $30R$. They claimed that the streamwise mean velocity profiles followed a power law in the overlap region and observed a clear scale separation between inner- and outer-scale turbulence. So far, the largest DNS of pipe flow is done at $Re_\tau \approx 6000$ with a relatively short length ($L_z = 15R$) by Pirozzoli *et al.* (2021) based on a lower-order numerical method.

In general, one would anticipate that various simulations and experiments to agree with each other to a high degree. However, a comparison among several datasets in spatially developing turbulent boundary layers (Schlatter & Örlü 2010), channels (Lee & Moser 2015), and pipes (Pirozzoli *et al.* 2021) flows surprisingly shows considerable variations among the various DNSs, even for basic measures such as the shape factor, friction coefficient, the von Kármán constant, etc. Accurate turbulence statistics are very much needed, both for understanding turbulence physics and for developing, adapting and validating turbulence models. Here, we present a new high-fidelity DNS dataset of turbulent pipe flow generated with a pseudo-spectral method for Re_τ up to 5200 and with the axial length $L_z/R = 10\pi$, which is

| Re_τ | Re_b | $N_z \times N_r \times N_\theta$ | Δz^+ | Δr_w^+ | Δr_{max}^+ | $\Delta(R\theta)^+$ | Tu_τ/R | Symbols |
|-----------|--------|----------------------------------|--------------|----------------|--------------------|---------------------|-------------|---------|
| 181 | 5300 | $1024 \times 192 \times 256$ | 5.5 | 0.02 | 2.0 | 4.4 | 105.3 | ▣ |
| 549 | 19,000 | $2048 \times 256 \times 768$ | 8.4 | 0.09 | 3.2 | 4.5 | 24.7 | ⊙ |
| 998 | 37700 | $3072 \times 384 \times 1280$ | 10.2 | 0.1 | 3.9 | 4.9 | 17.1 | ▽ |
| 2001 | 83000 | $6144 \times 768 \times 2560$ | 10.2 | 0.1 | 3.9 | 4.9 | 9.7 | △ |
| 5197 | 240000 | $12288 \times 1024 \times 5120$ | 12.8 | 0.2 | 8.6 | 6.3 | 4.6 | ★ |

Table 1: Summary of simulation parameters. The axial length of the pipe (L_z) is $10\pi R$, with R being the pipe radius. Here, $Re_\tau (\equiv u_\tau R/\nu)$ and $Re_b (\equiv 2U_b R/\nu)$ are the frictional and bulk Reynolds numbers, respectively. N_z and N_θ are the number of dealiased Fourier modes in axial and azimuthal directions, and N_r are the number of grid points in the radial direction. Δz and $\Delta(R\theta)$ are the grid spacing in the axial and azimuthal directions, defined in terms of the Fourier modes. In the radial direction, Δr_w^+ represents the grid spacing at the wall, and Δr_{max}^+ denotes the maximum grid spacing. Tu_τ/R is the total eddy-turnover times without the initial transient phase.

long enough to capture the LSMs and VLSMs reported in experimental studies (Guala *et al.* 2006). The accuracy of this dataset is quantified by using the newly developed uncertainty quantification method. In addition, the dataset is extensively compared with other DNS and experimental data for turbulent pipe and channel flows.

2. Simulation details

DNSs of incompressible turbulent pipe flows are performed using the pseudo-spectral code “OPEN-PIPEFLOW” developed by Willis (2017). The radial, axial, and azimuthal directions are represented by r , z , and θ , and the corresponding velocity components are u_r , u_z , and u_θ . Fourier discretization is employed in the periodic axial (z) and azimuthal (θ) directions, while a central finite difference scheme with a nine-point stencil is adopted in the radial (r) direction. The number of grid points in r -direction is N_r , and the number of Fourier modes in z - and θ -directions are N_z and N_θ , respectively. In the physical space, the number of grid points in the z - and θ -directions increases by a factor of $3/2$ due to dealiasing. Grid points are distributed in r -direction according to a hyperbolic tangent function so that high wall-normal velocity gradients in the viscous sublayer can be resolved. In addition, the first few points near $r = 0$ are also clustered to preserve the high order of the finite difference scheme across the pipe axis. The governing equations are integrated with a second-order semi-implicit time-stepping scheme. The flow is driven by a pressure gradient, which varies in time to ensure that the mass flux through the pipe remains constant. For more details about the code and the numerical methods, see Willis (2017).

Five different Reynolds numbers $Re_\tau \approx 180, 550, 1000, 2000,$ and 5200 are considered. The detailed simulation parameters, such as domain sizes and grid sizes, etc. are listed in Table 1. The simulations are performed with resolutions that are comparable to those used in the prior simulations, e.g. Lozano-Durán & Jiménez (2014) and Lee & Moser (2015). In particular, for $Re_\tau \leq 2000$, the axial and azimuthal resolutions employed here satisfy the criterion suggested by Yang *et al.* (2021) for capturing 99% of the wall shear stress events. For the highest Re_τ case (i.e. ≈ 5200), $N_z = 12288$ and $N_\theta = 5120$ Fourier modes are used in the z - and θ -directions – corresponding to an effective resolution of $\Delta z^+ = L_x^+/N_z = 12.8$ and $\Delta(R\theta)^+ = (2\pi R^+)/N_\theta = 5.1$. Hereinafter, the superscript $+$ indicates non-dimensionalization in wall units, i.e. with kinematic viscosity ν and friction velocity u_τ . For comparison, several DNS and experimental data from the literature are included. The details are listed in table 2. To further validate the accuracy of our simulation, an additional simulation at $Re_\tau = 2000$ is performed using NEK5000 (hereinafter, this case is denoted as NEK5000 2K). The numerical setup and mesh generation are the same as those in El Khoury *et al.* (2013). The length of the pipe is chosen as $L_z = 35R$, and the total number of spectral elements is 7598080. With the polynomial order set to 12, the total number of grid points is approximately 13.1×10^9 . The grid spacing is comparable to that used in El Khoury *et al.* (2013) in all directions.

The uncertainty in the flow quantities due to the finite time-averaging is estimated using the methods described in Rezaeiravesh *et al.* (2022) and Xavier *et al.* (2022). For the central moments of velocity

| Reference | Type | Re_τ range | Method |
|-------------------------------------|---------------|-----------------|--------|
| Wu & Moin (2008) | DNS | 180,1140 | FD |
| El Khoury <i>et al.</i> (2013) | DNS | 180 – 1000 | SE |
| Chin <i>et al.</i> (2014) | DNS | 180 – 2000 | SE |
| Ahn <i>et al.</i> (2013, 2015) | DNS | 3000 | FD |
| Pirozzoli <i>et al.</i> (2021) | DNS | 180 – 6000 | FD |
| Furuichi <i>et al.</i> (2015, 2018) | EXP | 1000 – 53000 | LDV |
| Lee & Moser (2015) | DNS (channel) | 180 – 5200 | SB |
| Hoyas <i>et al.</i> (2022) | DNS (channel) | 10000 | SC |

Table 2: List of references of data used. FD denotes finite difference, SE denotes spectral element, SB denotes spectral/B-spline, SC denotes spectral/compact finite difference, and LDV represents laser Doppler velocimetry.

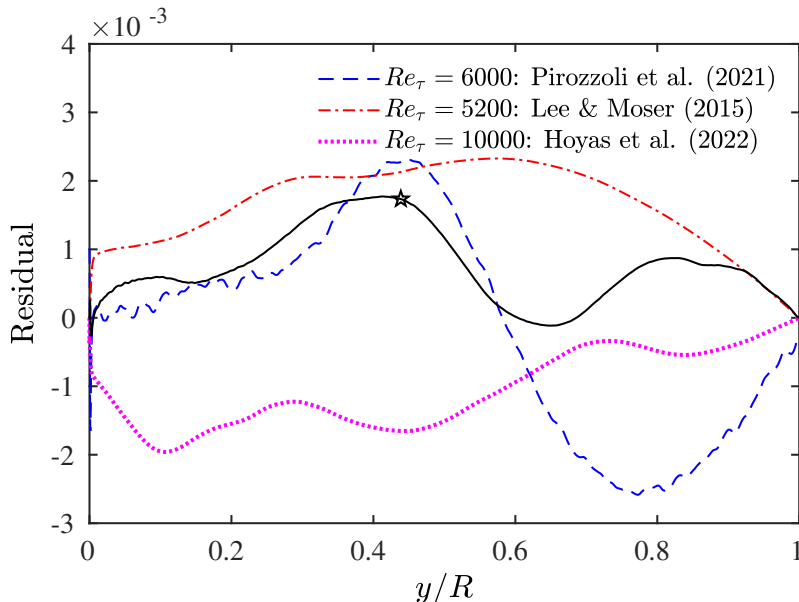


Figure 1: Comparison of the residual in the mean momentum equation (2.1) among different high Re simulations. The black solid line with star denotes our $Re_\tau = 5200$ result.

and pressure, the central limit theorem is applied to the time samples averaged over the z - and θ -directions. The associated time-averaging uncertainty is estimated using an autoregressive-based model for the autocorrelation function, see e.g. Oliver *et al.* (2014) and Xavier *et al.* (2022). For estimating the uncertainty in the combination of central moments, the method proposed by Rezaeiravesh *et al.* (2022) is employed. See Appendix A for further discussion on the method and estimated uncertainties in the first- and second-order velocity moments. For $Re_\tau = 5200$ case, the estimated standard deviation of the mean axial velocity (U^+) is less than 0.1%, and the estimated standard deviation of the velocity variance (i.e. $\langle u_r'^2 \rangle^+$, $\langle u_\theta'^2 \rangle^+$, $\langle u_z'^2 \rangle^+$) and covariance ($\langle u_r' u_z' \rangle^+$) is less than 1% in the near-wall region ($y^+ < 100$) and about 5% in the center region. Hereinafter, the velocity fluctuations are denoted using the prime symbol (e.g. u_r'), and the ensemble (both in time and space) averaged quantities of the mean velocity and velocity fluctuations are expressed using a capital letter or bracket (e.g. U or $\langle u_r' u_\theta' \rangle^+$).

In addition, the mean momentum equation is employed to ensure that the simulation is statistically stationary. Due to momentum balance, the total stress, which is the sum of Reynolds shear stress $\langle u_r' u_\theta' \rangle^+$ and mean viscous stress $\partial U^+ / \partial y^+$, is linear in a statistically stationary turbulent pipe flow:

$$\frac{\partial U^+}{\partial y^+} - \langle u_r' u_\theta' \rangle^+ = 1 - y/R, \quad (2.1)$$

| Re_τ | $10^2 \lambda$ | $\langle u_z'^2 \rangle_p^+$ | $-\langle u_r' u_z' \rangle_p^+$ | $\langle \tau_{z,w}'^2 \rangle^+$ | $\langle \tau_{\theta,w}'^2 \rangle^+$ | $p_{w,rms}^+$ | $p_{p,rms}^+$ |
|-----------|----------------|------------------------------|----------------------------------|-----------------------------------|--|---------------|---------------|
| 181 | 3.730(0.20%) | 7.229(0.41%) | 0.719(0.34%) | 0.123(0.54) | 0.031(1.18%) | 1.721(1.10%) | 2.039(0.90%) |
| 549 | 2.672(0.10%) | 7.587(0.14%) | 0.861(0.13%) | 0.158(0.14%) | 0.063(0.34%) | 2.283(0.62%) | 2.720(0.69%) |
| 998 | 2.244(0.14%) | 7.978(0.23%) | 0.902(0.13%) | 0.170(0.14%) | 0.071(0.15%) | 2.569(0.50%) | 3.020(0.38%) |
| 2001 | 1.859(0.22%) | 8.522(0.14%) | 0.932(0.14%) | 0.184(0.18%) | 0.079(0.18%) | 2.793(0.67%) | 3.273(0.54%) |
| 5197 | 1.498(0.24%) | 9.117(0.21%) | 0.957(0.12%) | 0.196(0.16%) | 0.082(0.28%) | 3.174(0.80%) | 3.610(0.70%) |

Table 3: Summary of values and standard deviation of some key parameters: the friction factor $\lambda = 8\tau_{z,w}/(\rho U_b^2)$; the peak of axial velocity variance $\langle u_z'^2 \rangle_p^+$; the peak of the Reynolds shear stress $-\langle u_r' u_z' \rangle_p^+$; the axial $\langle \tau_{z,w}'^2 \rangle^+$ and azimuthal $\langle \tau_{\theta,w}'^2 \rangle^+$ wall shear stress fluctuations; and the wall ($p_{w,rms}^+$) and peak ($p_{p,rms}^+$) values of root-mean-square (r.m.s.) pressure fluctuations.

here $y = R - r$. Figure 1 shows the residual in (2.1) for the $Re_\tau \approx 5200$ case. The discrepancy between the analytic linear profile (i.e. $1 - y/R$) and total stress profile (i.e. $\partial U^+/\partial y - \langle u_r' u_\theta' \rangle^+$) from the simulation is less than 0.002 in wall units and is comparable to other high- Re DNS in the literature. Note that this discrepancy is much smaller than the standard deviation of the estimated total stress (see appendix A).

3. Results

3.1. Flow visualization

The Re effect on the flow structure is qualitatively illustrated in figure 2, showing cross-sectional views of the instantaneous axial velocity u_z . Although large scales dominate in the central region of the pipe for all Re_τ cases, there is a general increase in the range of scales with increasing Re_τ . The average spacing between near-wall low-speed streaks is around $(R\theta)^+ = 100$. For the lowest Re_τ studied here, about ten evenly distributed low-speed structures are seen in figure 2(a), identified by the plume-shaped black regions ejecting from the wall. For our highest Re_τ , the streak spacing is reduced to about $0.02R$, and these fine-scale streaks can hardly be identified from the full cross-section in figure 2(e). A zoomed-in view of the near-wall region with domain size (1000, 200) in wall units in (r, θ) directions is provided to better visualize these structures, which share quite similar patterns as those in low Re_τ cases.

3.2. Friction factor

The mean friction (or wall-shear stress), which is proportional to the pressure drop or the amount of energy required to sustain the flow, is an important parameter and has been extensively studied (Blasius 1913; McKeon *et al.* 2005; Furuichi *et al.* 2015; Pirozzoli *et al.* 2021). A semi-empirical relation between the friction factor $\lambda = 8\tau_{z,w}/(\rho U_b^2)$ and Re is given as (known as the Prandtl friction law):

$$1/\lambda^{1/2} = A \log_{10}(Re_b \lambda^{1/2}) - B, \quad (3.1)$$

where the constant A is related to the von Kármán constant as $A = 1/(2\kappa\sqrt{2}\log_{10}(e))$. Curve-fitting the experimental data over $3.1 \times 10^3 < Re_b < 3.2 \times 10^6$ by Nikuradse (1933) yields $A = 2.0$ and $B = 0.8$, which corresponds to $\kappa = 0.407$. However, notable deviations were observed when comparing the Prandtl friction law with other experimental data. For example, McKeon *et al.* (2005) showed that for the Princeton Superpipe data (in the range of $3.1 \times 10^4 \leq Re_b \leq 3.5 \times 10^7$), the constants of the Prandtl law work only over a limited range of Re_b . New constants (i.e. $A = 1.920$ and $B = 0.475$) and additional Re -dependent corrections need to be introduced to better fit the data in the entire Re_b range. For the ‘‘Hi-Reff’’ data, Furuichi *et al.* (2015) found that λ deviates from the Prandtl law with approximately 2.5% in the lower Re_b and -3% in the high Re_b region. In addition, λ , although agreeing with the Superpipe data in the low Re_b range, deviates for $Re_b > 2 \times 10^5$.

Figure 3(a) shows the friction factor λ as a function of Re_b , along with other DNS and experimental data as well as the theoretical prediction λ_p based on (3.1). All DNS and experimental data seem to follow λ_p . However, the scatter is better highlighted by examining the relative error with respect to the Prandtl law (i.e. $\lambda/\lambda_p - 1$). As depicted in figure 3(b), all DNS data overshoot λ_p at the low Re_b (i.e.

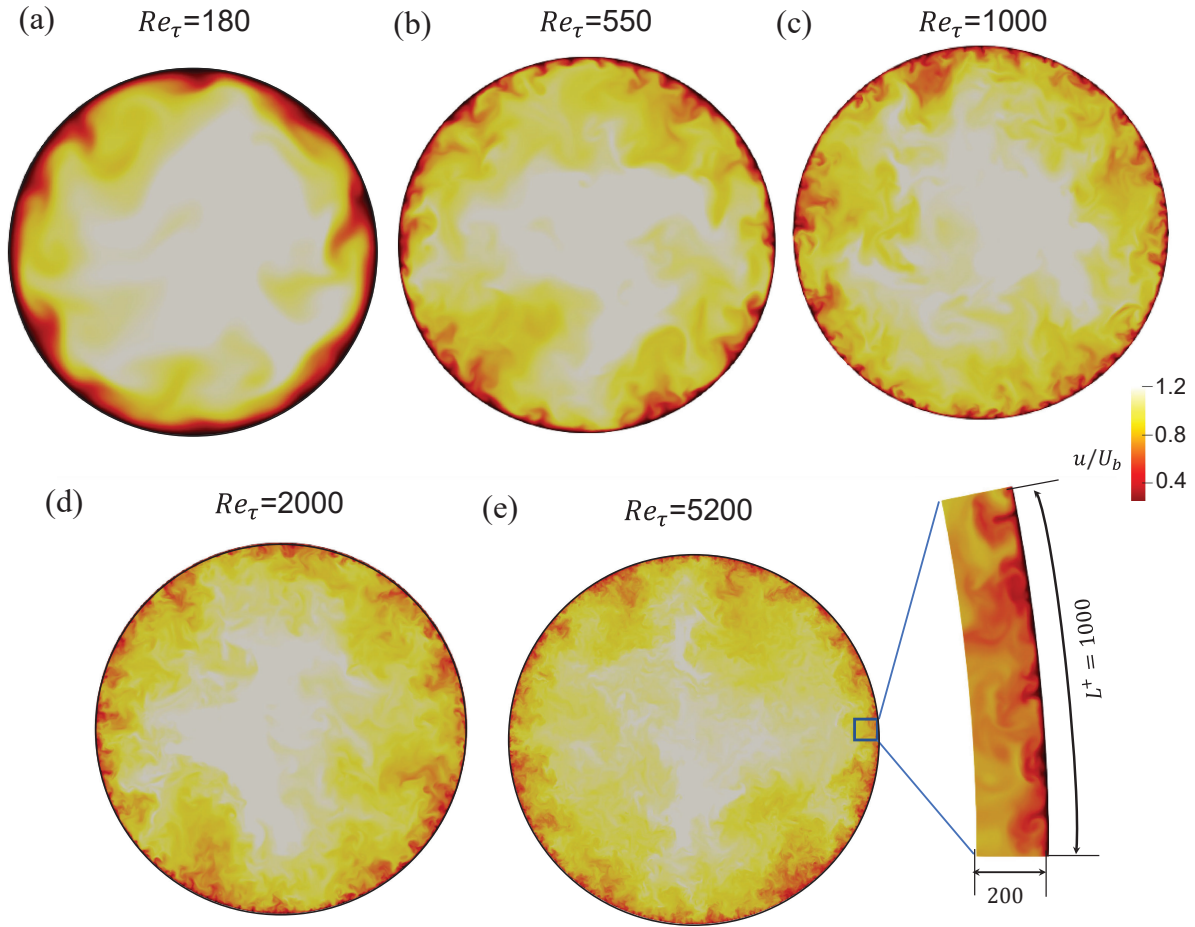


Figure 2: Visualization of the instantaneous axial velocity u_z/U_b for (a) $Re_\tau = 180$, (b) 550, (c) 1000, (d) 2000, and (e) 5200.

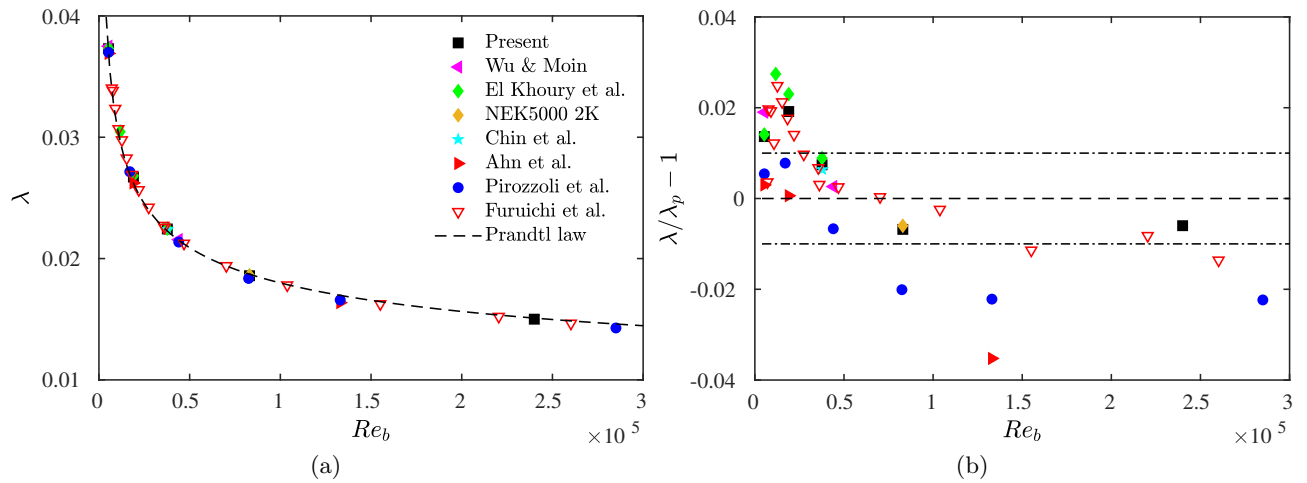


Figure 3: Friction factor λ as a function of Re_b and (b) the relative deviations from the Prandtl friction law.

$\leq 4 \times 10^4$). Our data, which agrees with Wu & Moin (2008); El Khoury *et al.* (2013); Chin *et al.* (2014) and the new simulation at $Re = 2000$ using NEK5000, exceed λ_p by about 2%, while the results of Ahn *et al.* (2013) and Pirozzoli *et al.* (2021) are closer to λ_p (within 1% for $Re_b < 5 \times 10^4$). Pirozzoli *et al.* (2021) attributed this discrepancy to the different grid resolutions employed in the θ -direction, which is $(R\theta)^+ = 4-5$ in theirs and Ref. Ahn *et al.* (2013), but 7–8 for Wu & Moin (2008) and Chin *et al.* (2014). However, the data from El Khoury *et al.* (2013) and our DNS have comparable azimuthal resolutions as Ahn *et al.* (2013) and Pirozzoli *et al.* (2021) but produce results similar to Wu & Moin (2008) and Chin *et al.* (2014) – suggesting that the azimuthal resolution is not the main reason for such discrepancy. Interestingly, the data of Ahn *et al.* (2013) and Pirozzoli *et al.* (2021) are consistently lower than our and other results in the whole Re_b range. In particular, at the highest Re_b , Pirozzoli *et al.* (2021)'s data undershoots by 2% from λ_p , but our data is lower by only about 0.6%. Table 3 asserts that such differences in λ are beyond the uncertainty limit. We speculate that the discrepancy is due to the numerical methods used – second-order finite difference for Ahn *et al.* (2013) and Pirozzoli *et al.* (2021), and higher-order methods for others.

Our DNS and the experimental data by Furuichi *et al.* (2015) agree well for the Re_b range studied. Fitting our DNS data with (3.1) yields $A = 2.039 \pm 0.083$, $B = 0.948 \pm 0.364$ with uncertainty estimates based on 95% confidence bounds, giving $\kappa = 0.399 \pm 0.015$. The value reported by Pirozzoli *et al.* (2021) (i.e. $A = 2.102$, $B = 1.148$) are slightly larger than ours but still within the uncertainty range. However, large uncertainty is present in the fitted values due to the limited data points in Re . In addition, as the Re_b is still relatively low, the reported value of $\kappa = 0.399 \pm 0.015$ should not be used outside of the given Reynolds number range. As will be shown in section 3.4, even for the highest Re_b case, a distinct logarithmic region does not manifest itself in the mean velocity profile $U(y)$. Higher Re data is required to better estimate the constants in (3.1) and the associated κ values.

3.3. Wall shear stress fluctuations

The Re -dependence of axial wall-shear stress fluctuation $\langle \tau_{z,w}^{\prime 2} \rangle^+$ is one of the highly debated issues in wall turbulence. Note that $\langle \tau_{z,w}^{\prime 2} \rangle^+$ is also equivalent to the wall dissipation of the axial Reynolds stress components $\epsilon_{z,w}^+$, the azimuthal vorticity variance at the wall $\langle \omega_\theta^{\prime 2} \rangle^+$ or the limiting value of $\langle u_z^{\prime 2} \rangle^+ / U^2$ at the wall (Örlü & Schlatter 2011). Previous DNS studies on channel, pipe, and turbulent boundary layer observed an increase in $\langle \tau_{z,w}^{\prime 2} \rangle^+$ with Re_τ , which reflects the increased contribution of large-scale motions on wall shear stress at high Re 's (Marusic *et al.* 2010a). However, the exact dependence of $\langle \tau_{z,w}^{\prime 2} \rangle^+$ on Re_τ is not well established. For example, Örlü & Schlatter (2011) suggested that the r.m.s. $\langle \tau_{z,w}^{\prime 2} \rangle^+$ follows

$$\langle \tau_{z,w}^{\prime 2} \rangle^{+1/2} = C + D \ln(Re_\tau), \quad (3.2)$$

where the two constants C and D are chosen as 0.298 and 0.018 based on the DNS of turbulent boundary layer data.

Some works (Yang & Lozano-Durán 2017; Smits *et al.* 2021) also suggested that

$$\langle \tau_{z,w}^{\prime 2} \rangle^+ = E + F \ln(Re_\tau), \quad (3.3)$$

By fitting turbulent channel flow data of Lee & Moser (2015) and pipe flow data of Pirozzoli *et al.* (2021) for $Re_\tau \geq 1000$, Smits *et al.* (2021) obtained $E = 0.08$ and $F = 0.0139$.

Recently, Chen & Sreenivasan (2021) proposed a defect power law, given as

$$\langle \tau_{z,w}^{\prime 2} \rangle^+ = \epsilon_{z,w}^+ = G - H Re_\tau^{-1/4}, \quad (3.4)$$

where G is the asymptotic value at infinite Re , and H is the coefficient. The assumption for (3.4) is that the energy dissipation balances the turbulent kinetic energy production $P_k = -\langle u_r u_z \rangle^+ (\partial U^+ / \partial y^+)$ near the location of peak production. The fact that P_k is bounded by 1/4 (Sreenivasan 1989; Pope 2000) implies that the wall dissipation $\epsilon_{z,w}^+$ may also stay bounded, which is further assumed by Chen & Sreenivasan (2021) to be the same bound as P_k , i.e. $G = 1/4$ (Chen & Sreenivasan 2021). This argument was later criticized by Smits *et al.* (2021) for the following two reasons. First, based on the DNS data, the location of peak production is actually the place where the largest imbalance of production and dissipation occurs.

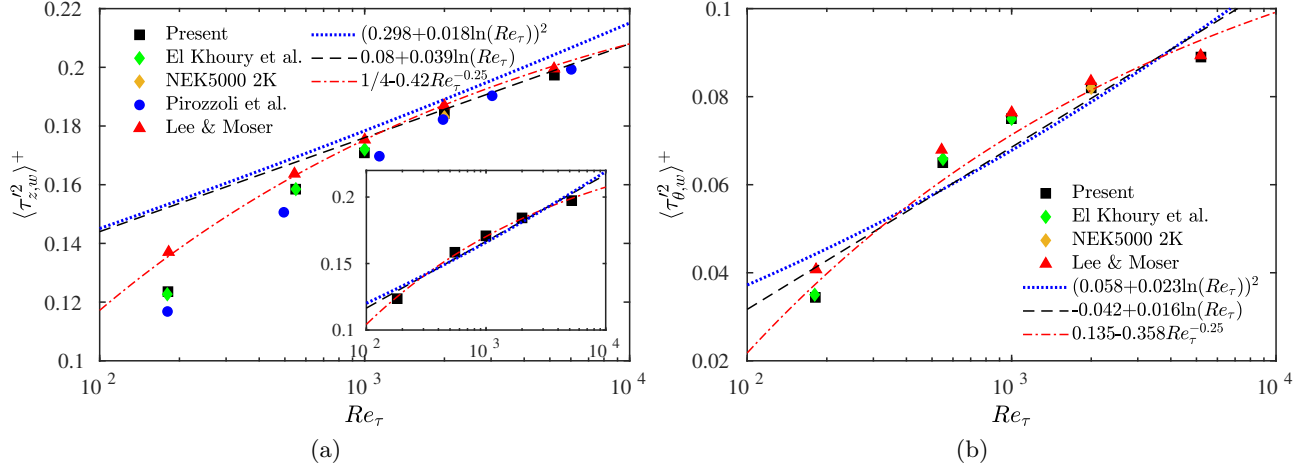


Figure 4: (a) Axial $\langle \tau_{z,w}^{\prime 2} \rangle^+$ and (b) azimuthal $\langle \tau_{\theta,w}^{\prime 2} \rangle^+$ wall shear stress fluctuations as a function of Re_τ . The dotted, dashed and dashed-dotted lines in the inset of (a) denote $\langle \tau_{z,w}^{\prime 2} \rangle^+ = (0.225 + 0.0264 \ln(Re_\tau))^2$, $\langle \tau_{z,w}^{\prime 2} \rangle^+ = 0.016 + 0.0218 \ln(Re_\tau)$ and $\langle \tau_{z,w}^{\prime 2} \rangle^+ = 0.255 - 0.477 Re_\tau^{-1/4}$, respectively.

Second, as the balance between different terms in the Reynolds stress transport equation rapidly changes near the wall, it is unclear how the balance between P_k and $\epsilon_{z,w}^+$ can be extended up to the wall, where $P_k = 0$, and $\epsilon_{z,w}^+$ equals the viscous diffusion.

The axial wall-shear stress fluctuation $\langle \tau_{z,w}^{\prime 2} \rangle^+$ as a function of Re_τ is depicted in figure 4(a). Akin to the observation in El Khoury *et al.* (2013), the values for the pipe are slightly lower than those for the channel, but the difference decreases with increasing Re_τ . Note that the data of Pirozzoli *et al.* (2021) is slightly lower than others, which is consistent with the lower λ in figure 3. The logarithmic law (3.2) proposed by Örlü & Schlatter (2011) is higher than the DNS data. This is somehow expected as the fitting coefficients were obtained based on the DNS of turbulent boundary layer data, which is higher than pipe and channels. In the high Re_τ range, both the logarithmic (3.3) and defect power law scaling (3.4) agree well with the data. However, both scalings exhibit notable disagreements in the low Re_τ range. The discrepancy seems not particularly surprising, given that the parameters in these equations are obtained from different datasets and different Re_τ ranges. As a reference, the inset in figure 4(a) shows the fitting results of (3.2) – (3.4) using our DNS data only. The fitted values are $C = 0.225$, $D = 0.0264$ for (3.2), $E = 0.016$, $F = 0.0218$ for (3.3) and $G = 0.255$, $H = 0.477$ for (3.4). For the Re_τ range studied, the data seem to match better the defect power law but with a slightly higher asymptotic value than suggested by Chen & Sreenivasan (2021). Additional data at even higher Re_τ is needed to confirm this finding.

Figure 4(b) further shows the azimuthal wall shear stress fluctuation $\langle \tau_{\theta,w}^{\prime 2} \rangle^+$ as a function of Re_τ . Similar to that found for $\langle \tau_{z,w}^{\prime 2} \rangle^+$, our data agree well with El Khoury *et al.* (2013) and NEK5000 2K cases, and all of them become closer to Lee & Moser (2015) with increasing Re_τ . Fitting data with the logarithmic and defect power law yields $\langle \tau_{\theta,w}^{\prime 2} \rangle^+ = (0.058 + 0.023 \ln(Re_\tau))^2$, $\langle \tau_{\theta,w}^{\prime 2} \rangle^+ = -0.040 + 0.016 \ln(Re_\tau)$ and $\langle \tau_{\theta,w}^{\prime 2} \rangle^+ = 0.135 - 0.353 Re_\tau^{-1/4}$. Again, the defect power law seems to match better the DNS data, but the agreement is not as good as for $\langle \tau_{z,w}^{\prime 2} \rangle^+$.

3.4. Mean velocity profile

In an overlap region between the inner and outer flows, there is a logarithmic variation of the mean axial velocity U^+ profile, which is given as

$$U^+ = \frac{1}{\kappa} \ln y^+ + B. \quad (3.5)$$

In a true log layer, the indicator function $\beta = y^+(\partial U^+ / \partial y^+)$ is constant and equals $1/\kappa$.

The U^+ profiles at different Re_τ are compared to previous DNS data in figure 5(a). First, as expected, U^+

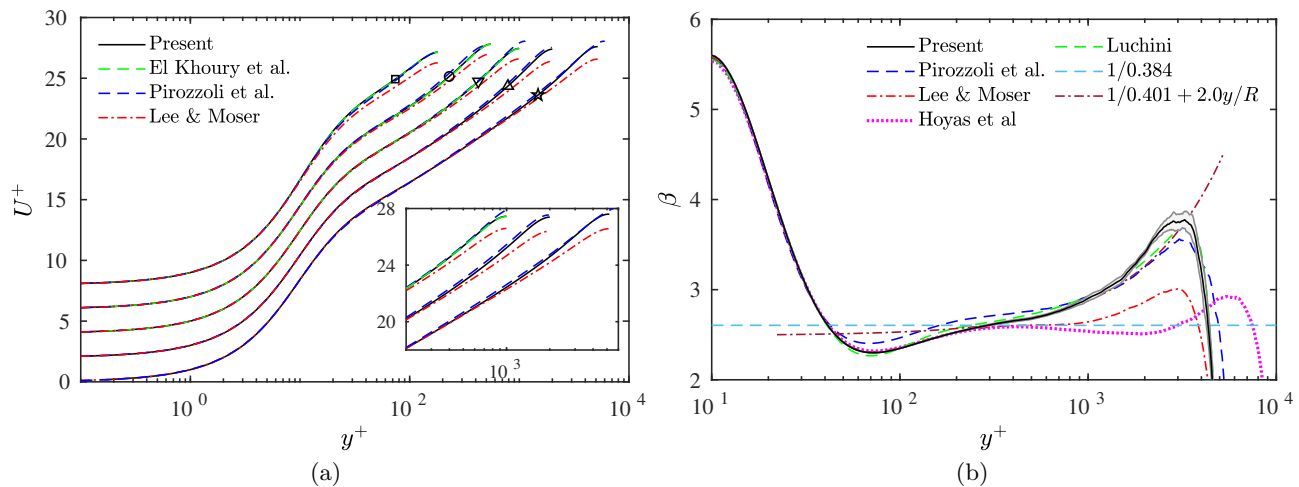


Figure 5: (a) Mean velocity profiles U^+ and (b) log-law diagnostic function β . Profiles in (a) are offset in the vertical direction by two wall units, and the shaded areas in (b) represents the standard deviation of our data at $Re_\tau = 5200$.

for pipe flows has a stronger wake when compared with the channel data by [Lee & Moser \(2015\)](#). Second, our data in the outer region agree well with [El Khoury et al. \(2013\)](#)'s, but not with [Pirozzoli et al. \(2021\)](#). This discrepancy was also noted by [Pirozzoli et al. \(2021\)](#), who found that their data, along with those of [Wu & Moin \(2008\)](#) and [Ahn et al. \(2013\)](#), differ from those of [El Khoury et al. \(2013\)](#) and [Chin et al. \(2014\)](#). Again, this disparity seems to be due to the numerical methods, where all of the former used low order finite-difference methods, while the latter used high-order spectral-element methods.

The log-law diagnostics function β is shown in figure 5(b) for all high DNS data (i.e. $Re_\tau > 5000$). Interestingly, β for our $Re_\tau = 5200$ agrees with the channel data by [Lee & Moser \(2015\)](#) and [Hoyas et al. \(2022\)](#) up to $y^+ \approx 250$. This suggests a near-wall universality of the inner scaled mean velocity – similar to that observed by [Monty et al. \(2009\)](#). For all three cases, the trough is $\beta \approx 2.30$, located at $y^+ \approx 70$. However, the data of [Pirozzoli et al. \(2021\)](#) deviates from others for $y^+ > 40$ and has a larger magnitude of the trough, which is somehow consistent with the slight upward shift of the U^+ observed in Fig 5(a). This discrepancy is significantly larger than the statistical uncertainty (Appendix A). Unlike channel flow, where a plateau starts to develop for $Re_\tau \geq 5200$, there is no plateau for pipe flow – suggesting that the minimum Re_τ for U^+ to develop a logarithmic region should be higher in the pipe than in the channel. The β in the wake component of the pipe is distinctly larger than the channel, implying a notable difference in flow structures in the core region between these two flows ([Chin et al. 2014](#)).

High order corrections to the log-law relation (3.5) were sometimes introduced to better describe the mean velocity profile in the overlap region ([Buschmann & Gad-el Hak 2003](#); [Luchini 2017](#); [Cantwell 2019](#)). For example, based on refined overlap arguments expressed by [Afzal & Yajnik \(1973\)](#), [Jiménez & Moser \(2007\)](#) proposed the following the indicator function

$$\beta = \left(\frac{1}{\kappa_\infty} + \frac{\alpha_1}{Re_\tau} \right) + \alpha_2 \frac{y}{R}, \quad (3.6)$$

where α_1 and α_2 are adjustable constants, and κ_∞ is the asymptotic von Kármán constant. (3.6) allows for a Re -dependence of $\kappa = \kappa_\infty + (\alpha_1/Re_\tau)^{-1}$ and introduces a linear dependence on y . By fitting our $Re_\tau = 5200$ data in the region between $y^+ = 300$ and $y = 0.16$, we obtain $\kappa = 0.401$ and $\alpha_2 = 2.0$. This κ is very close to 0.399 estimated from the friction factor relation (3.1) and 0.402 reported by [Jiménez & Moser \(2007\)](#) using channel data of $Re_\tau = 1000$ from [Del Alamo et al. \(2004\)](#) and $Re_\tau = 2000$ from [Hoyas & Jiménez \(2006\)](#). It is slightly larger than 0.387 by [Pirozzoli et al. \(2021\)](#) and 0.384 by [Lee & Moser \(2015\)](#). In addition, α_2 is generally much larger in the pipe than in channel flow – suggesting a strong geometry effect on β . The value of $\alpha_2 = 2$ is consistent with the finding by [Luchini \(2017\)](#), who suggested that the logarithmic law of the velocity profile is universal across different geometries of wall turbulence,

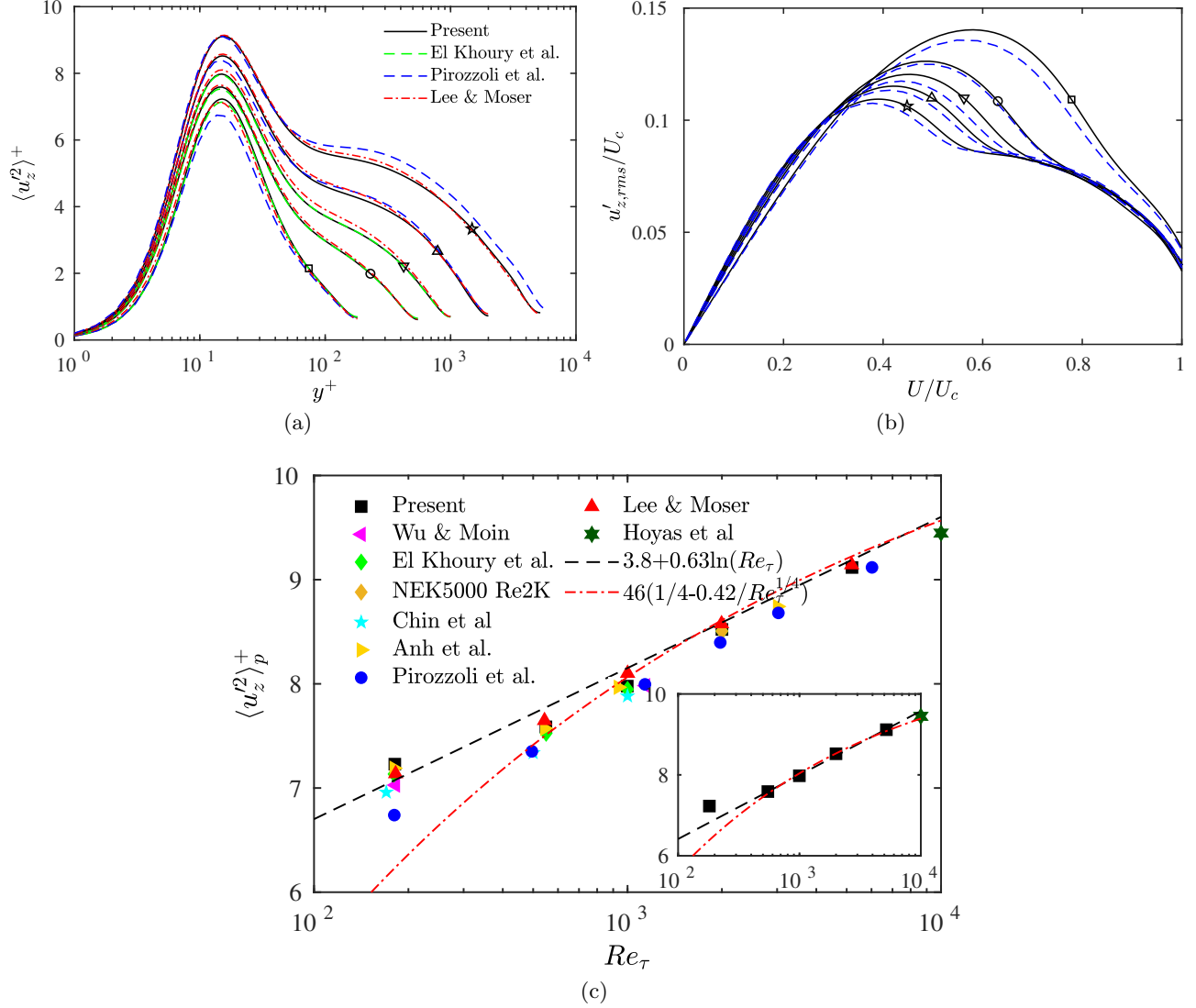


Figure 6: (a) Axial velocity variance $\langle u_z'^2 \rangle^+$ as a function of y^+ ; (b) the diagnostic plot depicting $u'_{z,rms}/U_c$ as a function of U^+/U_c , and (c) the inner peak of axial velocity variance $\langle u_z'^2 \rangle_p^+$ as a function of y^+ . The dashed and dashed-dotted lines in the insert of (c) denote $\langle u_z'^2 \rangle_p^+ = 3.251 + 0.687 \ln(Re_\tau)$ and $\langle u_z'^2 \rangle_p^+ = 11.132 - 17.402 Re_\tau^{-1/4}$, respectively.

provided the perturbative effect of the pressure gradient is taken into consideration. Furthermore, a good collapse can be observed between our data and the analytical prediction by Luchini (2017); see, figure 5(b).

3.5. Reynolds stresses

The non-zero components of the Reynolds stress tensor (or the velocity variances and covariance) are examined in this section (figures 6–9). For all datasets, the inner-scaled velocity variances and covariance increase with Re_τ in the whole wall-normal range. In terms of the axial velocity variance $\langle u_z'^2 \rangle^+$ (figure 6a), our data agrees well with El Khoury *et al.* (2013) but differs from Pirozzoli *et al.* (2021), which is notably smaller in the near wall region, particularly at low Re_τ . For the highest Re_τ cases, the agreement is reasonably good near the wall. However, note that Pirozzoli *et al.* (2021)'s simulation is at a slightly higher Re_τ (i.e. ~ 6000). The differences between our and Pirozzoli *et al.* (2021)'s cases can be better highlighted

in the diagnostic plot (figure 6b), where the root mean square (r.m.s.) axial velocity fluctuation $u'_{z,rms}$ is plotted against the mean velocity U^+ . The diagnostic plot was introduced by Alfredsson & Örlü (2010) as a means to assess if the mean velocity and velocity fluctuation profiles behave correctly without the need to determine the friction velocity or the wall position. Consistent with the observation in Alfredsson & Örlü (2010), the diagnostic plot collapses in the outer parts for $Re_\tau > 180$, and has a clear Re trend around the peak value. Most importantly, the data by Pirozzoli *et al.* (2021) is consistently lower than ours, particularly in the near-wall region. Such inconsistency is also observed for $\langle u_\theta'^2 \rangle^+$ (figure 9). The agreement for $\langle u_r'^2 \rangle^+$ (figure 7a) is reasonably good among different pipe flow datasets, which is slightly larger than the channel, particularly in the outer region. The Reynolds shear stress $\langle u_r' u_z' \rangle^+$ shows the best agreement among different datasets, even including the channel.

Let us focus now on the inner peak of the axial velocity variance $\langle u_z'^2 \rangle^+$. The inner peak is assumed to increase logarithmically with Re_τ – similar as the wall shear stress fluctuations due to the increased modulation effect of the large-scale structures in the logarithmic layer (Marusic & Monty 2019). Chen & Sreenivasan (2021) recently suggested that the growth of $\langle u_z'^2 \rangle^+$ would eventually saturate. The argument is based on the balance between the viscous diffusion and dissipation at the wall and the Taylor series expansion of the axial velocity variance near the wall, given as

$$\langle u_z'^2 \rangle^+ \sim D_{z,w}^+ y^{+2} = \epsilon_{z,w}^+ y^{+2}. \quad (3.7)$$

Note that a similar expression is obtained in Smits *et al.* (2021), where the axial wall dissipation is used instead, i.e. $\langle u_z'^2 \rangle^+ \sim \langle \tau_{z,w}'^2 \rangle^+ y^{+2}$. If the assumption of the boundness of wall dissipation (3.4) is valid and the inner peak location of $\langle u_z'^2 \rangle^+$ (denoted as $y_{z,p}^+$) is independent of Re_τ , then (3.7) suggests that the peak of axial velocity variance should also be bounded in a similar defect power form as the wall shear stress fluctuation:

$$\langle u_z'^2 \rangle_p^+ = M - N Re_\tau^{-1/4}, \quad (3.8)$$

where M is the asymptotic value and N is the coefficient.

This validity of (3.8) was recently challenged by Pirozzoli *et al.* (2021), who, based on their data, observed a slight increase of $y_{z,p}^+$ with Re_τ , from $y_{z,p}^+ = 14.28$ for $Re_\tau \approx 500$ to 15.14 for $Re_\tau \approx 6000$. We emphasize that such variation of $y_{z,p}^+$ with Re_τ is not observed in our case, where much finer near-wall resolutions are used than in Pirozzoli *et al.* (2021). The value of $y_{z,p}^+$ is approximately 15 for all Re_τ (e.g. $y_{z,p}^+ = 15.07, 15.03, 15.50$ for $Re_\tau = 180, 2000, \text{ and } 5000$, respectively) – akin to the findings by many others (Moser *et al.* 1999; Jiménez *et al.* 2010; Chin *et al.* 2014; Smits *et al.* 2021)).

Figure 6(c) shows the $\langle u_z'^2 \rangle_p^+$ for all the DNS data listed in table 2, along with the logarithmic law $\langle u_z'^2 \rangle_p^+ = 3.8 + 0.64 \ln(Re_\tau)$ by Marusic *et al.* (2017) and the power law $\langle u_z'^2 \rangle_p^+ = 11.5 - 19.32 Re_\tau^{-1/4}$ by Chen & Sreenivasan (2021). The difference between different DNS datasets is relatively small, except for those from Pirozzoli *et al.* (2021), which are consistently lower than others for all Re_τ . Note that such discrepancy is much larger than the uncertainty (standard deviation), which is less than 0.5% (see table 3). Both the logarithmic and defect power laws fit well with the data at the high Re_τ range but have certain discrepancies at the low Re_τ . It suggests that there might exist a transitional scaling – similar to that found for the Reynolds shear stress (Chen *et al.* 2019). The parameters in these two scaling laws can be adjusted to better fit our dataset. The inset shows the fitting results for our data without the one at $Re_\tau = 180$: $\langle u_z'^2 \rangle_p^+ = 3.251 + 0.687 \ln(Re_\tau)$ and $\langle u_z'^2 \rangle_p^+ = 11.132 - 17.402 Re_\tau^{-1/4}$. With these new constants, the agreement is improved for both scaling laws. In summary, for the Re_τ range studied, both scaling laws can provide good match with $\langle u_z'^2 \rangle_p^+$ data when the fitting parameters are properly adjusted. Data at even higher Re_τ is required to determine which law is more consistent with the data.

According to Townsend's attached eddy hypothesis, at sufficiently high Re , the Reynolds stress com-

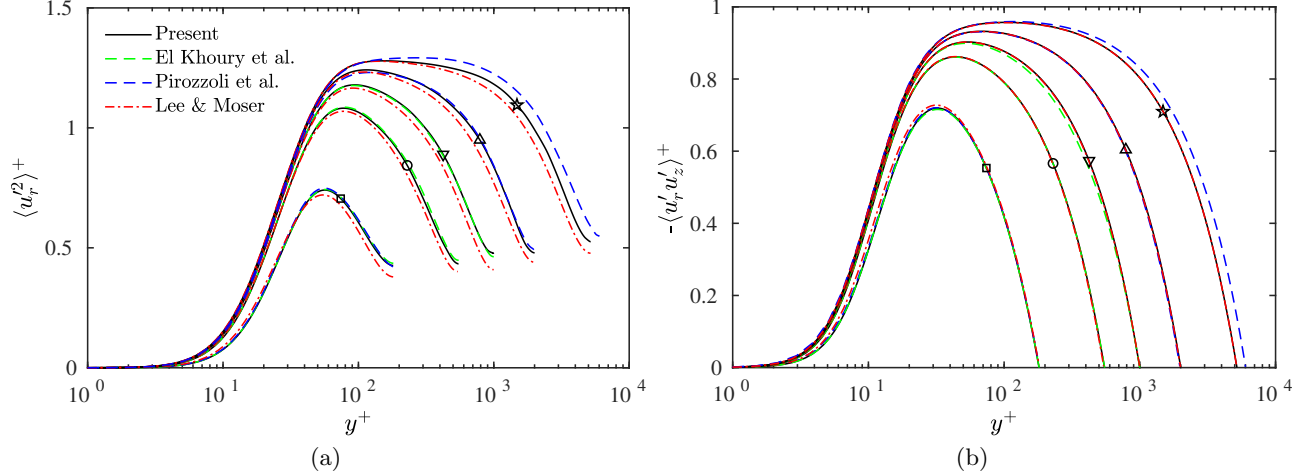


Figure 7: (a) Radial velocity variance $\langle u_r'^2 \rangle^+$ and (b) Reynolds shear stress $\langle u_r' u_z' \rangle^+$ as a function of y^+ .

ponents in a certain y range satisfy

$$\langle u_z'^2 \rangle^+ = A_1 - B_1 \ln(y/R), \quad (3.9)$$

$$\langle u_z'^2 \rangle^+ = A_2, \quad (3.10)$$

$$\langle u_\theta'^2 \rangle^+ = A_3 - B_3 \ln(y/R), \quad (3.11)$$

$$\langle u_r' u_z' \rangle^+ = -1, \quad (3.12)$$

where A_i and B_i are universal constants.

Consistent with these relations, the radial velocity variance $\langle u_r'^2 \rangle^+$ slowly develops a flat region as Re_τ increases. In addition, the Reynolds shear stress $\langle -u_r' u_z' \rangle^+$ profiles also tend to become flattened at higher Re_τ . As noted by Afzal (1982), the peak Reynolds shear stress at high Re_τ follows $\langle -u_r' u_z' \rangle_p^+ \approx 1 - 2/\sqrt{\kappa Re_\tau}$, and the corresponding position y_m^+ shifts away from the wall following $y_m^+ \sim \sqrt{Re_\tau/\kappa}$. Chen *et al.* (2019) suggested that there is a non-universal scaling transition, where the peaks at low Re_τ scales as $\langle u_r' u_z' \rangle_p^+ \approx Re_\tau^{-2/3}$ and their locations scales as $y_m^+ \sim Re_\tau^{1/3}$. Figure 8 shows $\langle -u_r' u_z' \rangle_p^+$ and the corresponding y_m^+ as a function of Re_τ . For $Re_\tau > 1000$, the $Re^{-1/2}$ for $\langle -u_r' u_z' \rangle_p^+$ and $Re^{-1/2}$ for y_m^+ are satisfied with good accuracy, and at the low Re_τ range, the $Re_\tau^{-2/3}$ for $\langle -u_r' u_z' \rangle_p^+$ and $Re_\tau^{-1/3}$ for y_m^+ scalings proposed by Chen *et al.* (2019) also yield a good agreement.

Regarding the axial velocity variance $\langle u_z'^2 \rangle^+$, no clear logarithmic region is observed for the Re_τ range considered here. As discussed in Lee & Moser (2015), $Re_\tau = 5200$ is not quite high enough to exhibit such a region. Based on the Superpipe data, Marusic *et al.* (2013) suggested that a sensible logarithmic layer emerges only for $Re_\tau > 10^4$. Consistent with the findings in Lee & Moser (2015) and Pirozzoli *et al.* (2021), the azimuthal velocity variance $\langle u_\theta'^2 \rangle^+$ (figure 9b) develops the logarithmic layers even at lower Re_τ . Fitting the $Re_\tau = 5200$ data in the range between $0.02 \leq y \leq 0.2$ yields $A_3 = 0.921$, $B_3 = 0.420$, which is close to $A_3 = 1.0$, $B_3 = 0.40$ by Pirozzoli *et al.* (2021), and between $A_3 = 1.08$, $B_3 = 0.387$ obtained by Lee & Moser (2015) for the turbulent channel and $A_3 = 0.8$, $B_3 = -0.45$ by Sillero *et al.* (2013) in the turbulent boundary layer.

3.6. Production and dissipation of the turbulent kinetic energy

Figure 10(a) shows the production P_k^+ and dissipation ϵ_k^+ of the turbulent kinetic energy (i.e. $k^+ = (\langle u_r'^2 \rangle^+ + \langle u_\theta'^2 \rangle^+ + \langle u_z'^2 \rangle^+)/2$). Other terms in the transport equations of the turbulent kinetic energy and individual Reynolds stress components are available at <https://dataverse.tdl.org/dataverse/turbpipe>. The production P_k^+ has a peak at around $y^+ \approx 11$, and the corresponding magnitude approaches the asymptotic value $1/4$ as Re_τ increases. Despite notable differences in the mean axial/streamwise velocity

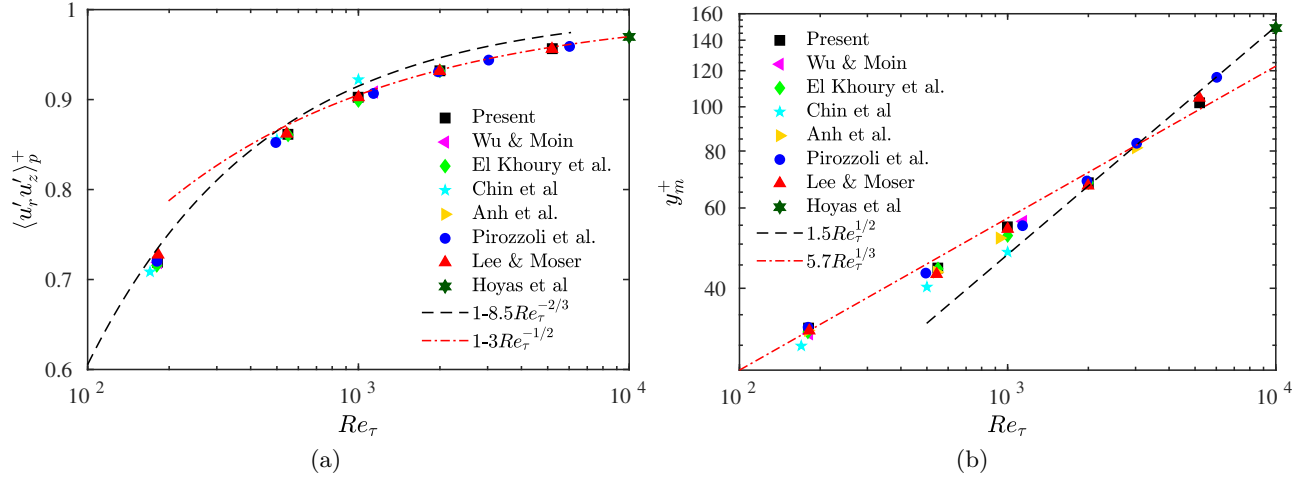


Figure 8: Reynolds number dependence of (a) the peak of the Reynolds shear stress $\langle u'_r u'_z \rangle^+$ and (b) the corresponding peak location in wall units.

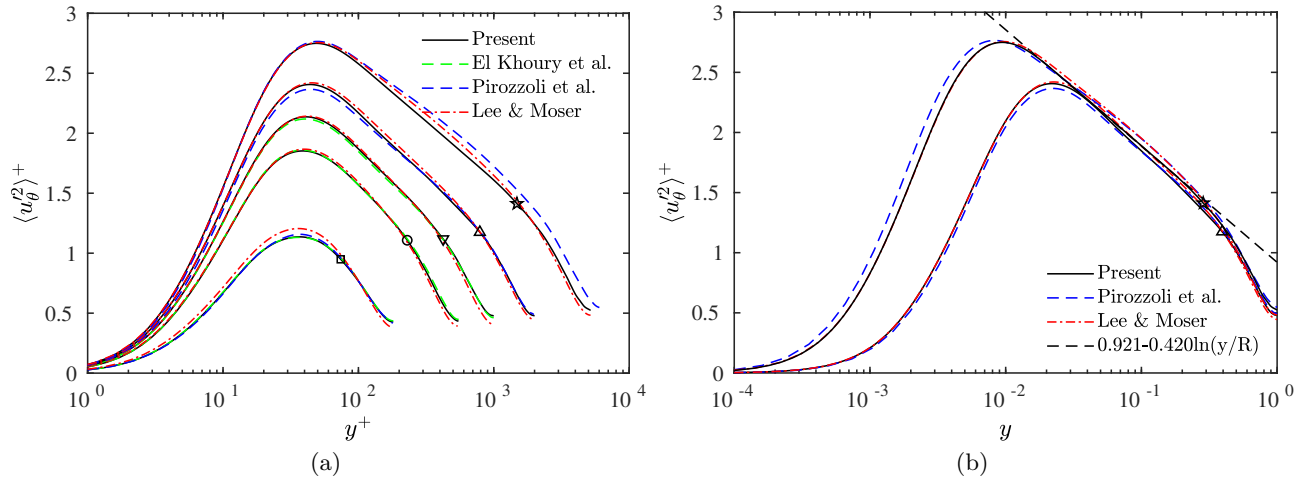


Figure 9: Azimuthal velocity variance $\langle u_\theta'^2 \rangle^+$ as a function of (a) y^+ and (b) y/R . Note that in (b) only the two highest Re_τ cases are included.

profile observed in the outer region, P_k^+ is quite similar between pipes and channels. It explains why the higher velocity gradient of the pipe does not contribute an effect to the turbulence intensities. The magnitude of dissipation ϵ_k^+ continuously increases with Re_τ , and the difference between the pipe and channel is mainly in the near wall region and decreases with increasing Re_τ .

At sufficiently high Re_τ , there is an intermediate region where the production balances the dissipation. Recent experimental (Hultmark *et al.* 2012) and numerical (Lee & Moser 2015; Pirozzoli *et al.* 2021) results suggest that such equilibrium between production and dissipation is violated due to the presence of LSMs and VLSMs. Figure 10(b) shows the relative excess of production over dissipation $(P_k^+/\epsilon_k^+ - 1)$. First, there is a near-wall region ($8 \leq y^+ \leq 35$), where P_k^+ distinctly exceeds the ϵ_k^+ . At high Re_τ , another region of $P_k^+/\epsilon_k^+ > 1$ develops, and the magnitude increases with Re_τ . For the $Re_\tau = 5200$ case, the peak imbalance is about 11% (located at $y^+ \approx 330$), which is slightly larger than in the channel (i.e. 8%)

3.7. Mean pressure and rms of pressure fluctuation

The mean pressure and r.m.s. pressure fluctuations are displayed in figure 11. First, the mean pressure P^+ has different behavior in the outer region between pipe and channel flows, with P^+ being substantially

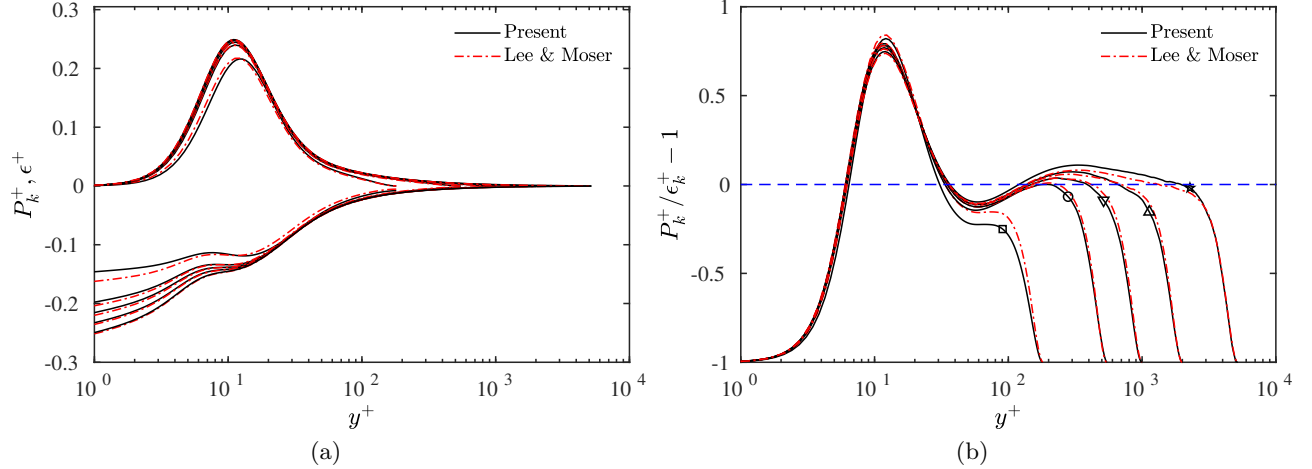


Figure 10: (a) Production P_k^+ and dissipation ϵ_k^+ of the turbulent kinetic energy, and (b) balance of production and dissipation $P_k^+/\epsilon_k^+ - 1$ as a function of y^+ .

lower in the wake of the pipe. As discussed in [El Khoury *et al.* \(2013\)](#), this difference is related to the mean radial momentum equation, which, in pipe flow, is given as ([Hinze 1975](#))

$$\frac{1}{\rho} \frac{\partial P}{\partial r} + \frac{d}{dr} \langle u_r'^2 \rangle + \frac{\langle u_r'^2 \rangle - \langle u_\theta'^2 \rangle}{r} = 0. \quad (3.13)$$

By changing variables (i.e. $r = R - y$) and then integrating the above equation, the mean pressure for pipe flow with the wall value set to zero can be expressed as

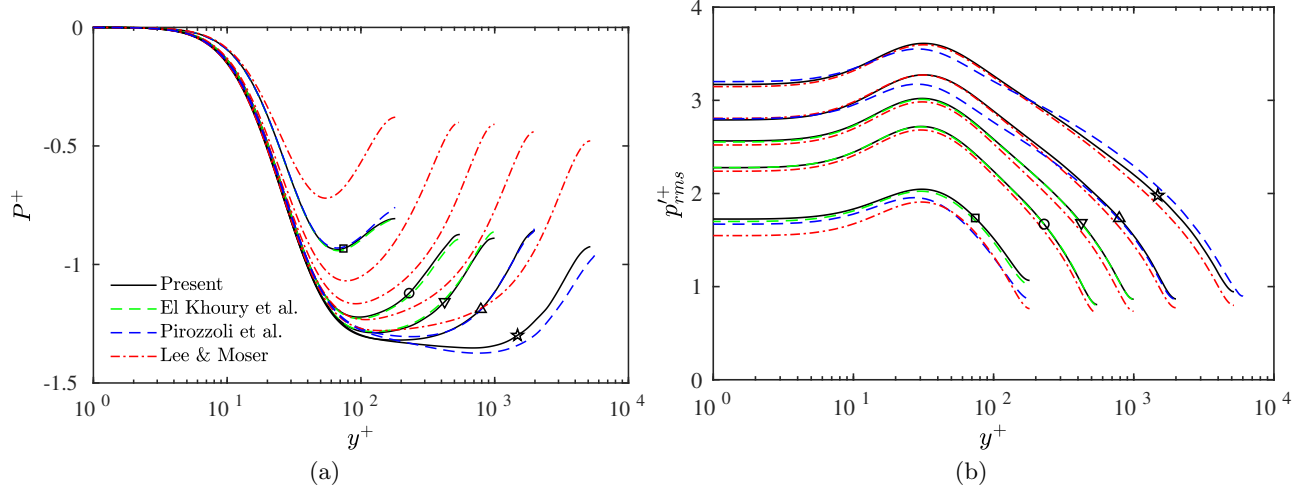
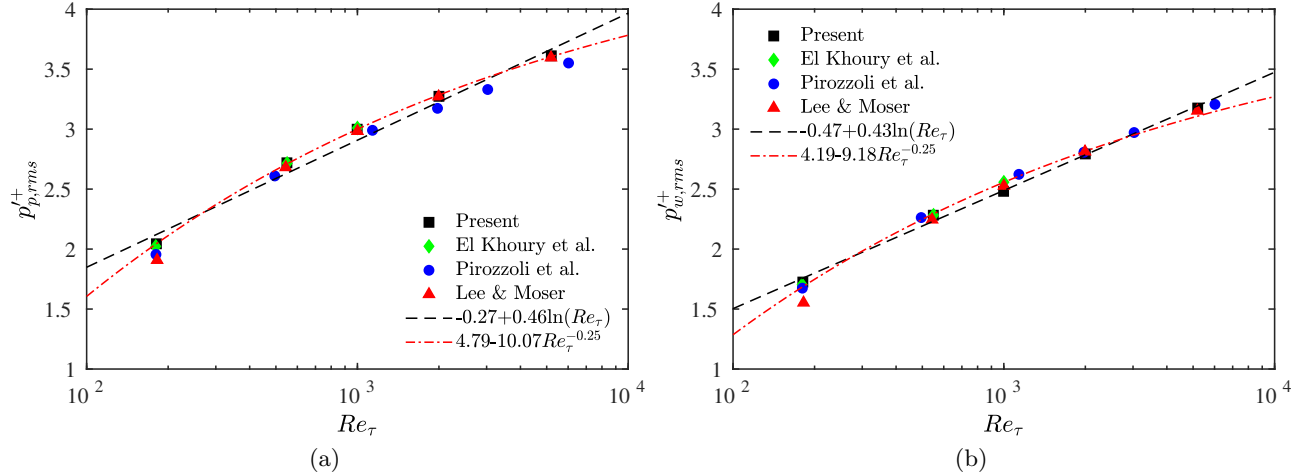
$$P^+(y) = -\langle u_r'^2 \rangle^+ + \int_0^y \frac{\langle u_r'^2 \rangle^+ - \langle u_\theta'^2 \rangle^+}{R - y'} dy'. \quad (3.14)$$

In channel flow, the last term on the left-hand side of (3.13) is absent, and the mean pressure is solely balanced by the wall-normal velocity fluctuation, i.e. $P^+(y) = -\langle v'^2 \rangle^+$. From figure 7(a), it is clear that the wall-normal velocity fluctuation is comparable between pipe and channel flows. However, as $\langle u_r'^2 \rangle^+ < \langle u_\theta'^2 \rangle^+$ in pipe flow, the extra term in (3.14) is zero at the wall and decreases with increasing y – resulting in a lower pressure in pipes than in channels.

Similar to that observed by [El Khoury *et al.* \(2013\)](#), the r.m.s. pressure fluctuation p_{rms}^+ exhibits similar behavior between the pipe and channel flows, except for slightly lower values for the latter. Minor differences are observed between our data and those of [Pirozzoli *et al.* \(2021\)](#), particularly near the peak value. The difference between our data with the channel data by [Lee & Moser \(2015\)](#) in the near-wall region decreases with increasing Re_τ . Figure 12 further shows the peak and wall values of p_{rms}^+ , which has similar Re -dependence as for other measures, such as wall shear stress fluctuations and axial velocity variances. Again, for the Re_τ studied, both the logarithmic and defect power laws fit the data well.

3.8. Energy spectra

As Re increases, the separation of scales between the near-wall and outer-layer structures enlarges. In this section, the separation of scales is examined with one-dimensional velocity spectra for $Re_\tau = 5200$ (figure 13). The energy spectra of axial velocity u_z in the axial direction has two distinct peaks – the inner one located at $k_z R = 40$ ($\lambda_z^+ = 816$) and $y^+ = 13$, and the outer one at $k_z R = 1$ ($\lambda_z = 2\pi R$), $y^+ = 400$. The dual peak is more discernible in the azimuthal spectra with peaks at $k_\theta = 250$ ($\lambda_\theta^+ = 2\pi r^+/k_\theta = 131$), $y^+ = 13$ and $k_\theta = 6$ ($\lambda_\theta = 2\pi r/k_\theta = 0.846R$), $y^+ = 1000$. The k_θ of all these peaks coincide with those found by [Lee & Moser \(2015\)](#) in the channel at the same Re_τ , but the physical scales are smaller than in the channel. It is well known that the inner peak at $y^+ = 13$ is associated with the streaks that are generated through the near-wall self-sustaining cycle ([Waleffe 1997](#); [Schoppa & Hussain 2002](#)). As

Figure 11: (a) Mean pressure (P^+) and (b) r.m.s. pressure fluctuation (p_{rms}^+) as a function of y^+ .Figure 12: Reynolds number dependence of (a) peak ($p_{p,rms}^+$) and (b) wall ($p_{w,rms}^+$) values of r.m.s. pressure fluctuations.

frequently seen in experiments (Monty *et al.* 2009; Hutchins & Marusic 2007; Rosenberg *et al.* 2013), the outer peak results from VLSMs. The outer peak in the θ -direction ($y = 0.192$) was located further away than the streamwise one ($y = 0.077$), which according to Wu *et al.* (2012) suggests that the VLSMs in the outer region maintain their energy in θ -direction stronger than the z -direction. The pre-multiplied energy spectra of the Reynolds shear stress in axial ($k_z E_{rz}/u_\tau^2$) and azimuthal ($k_\theta E_{rz}/u_\tau^2$) directions as a function of y^+ are shown in figures 13(c) and (d), respectively. The inner peak is located at $y^+ = 30$ with $k_z R = 49.2$ ($\lambda_\theta^+ = 664$) for $k_z E_{rz}/u_\tau^2$, and $k_\theta = 268$ ($\lambda_\theta^+ = 120$) for $k_\theta E_{rz}/u_\tau^2$. Compared with the axial velocity spectra, although the wavelength of the outer peak remains identical, the magnitude is much weaker and farther away from the wall.

Figure 14(a) shows the one-dimensional pre-multiplied energy spectra $k_z E_{zz}/u_\tau^2$ at different y locations. For comparison, the channel data of Lee & Moser (2015) at the same Re_τ is also included. First, good agreement is observed at $y^+ = 15$ between channel and pipe, particularly at higher wavenumbers – suggesting insignificance of pipe curvature to fine-scale near-wall structures. The scaling analysis of Perry *et al.* (1986) suggests that the energy spectral density of the axial velocity fluctuations $k_z E_{zz}/u_\tau^2$ should vary as k_z^{-1} in the overlap region. The k_z^{-1} region has previously been observed in the high Re experiments

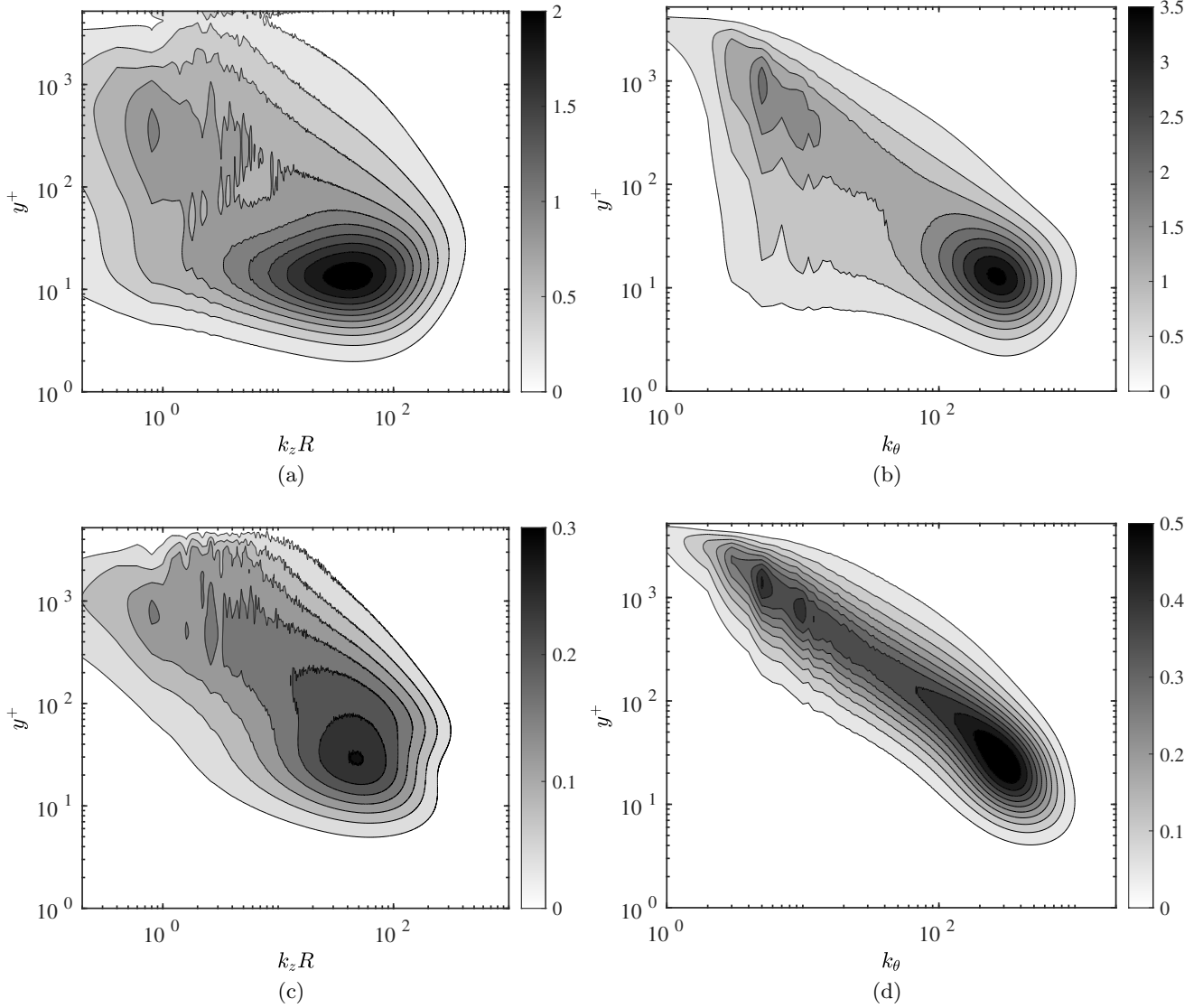


Figure 13: Wavenumber-premultiplied energy spectra for $Re_\tau = 5200$: (a) $k_z E_{zz}/u_\tau^2$; (b) $k_\theta E_{zz}/u_\tau^2$; (c) $k_z E_{rz}/u_\tau^2$; and (d) $k_\theta E_{rz}/u_\tau^2$.

(Nickels *et al.* 2005; Rosenberg *et al.* 2013). Recently, such k_z^{-1} has also been discovered in DNS of turbulent channel flow at $Re_\tau = 5200$ (Lee & Moser 2015). Similarly, a plateau in the region $6 \leq k_z R \leq 10$ is observed for $90 \leq y^+ \leq 170$, and the magnitude of 0.8 agrees with experiments (Nickels *et al.* 2005; Rosenberg *et al.* 2013). A bimodal is observed for $y^+ = 90$, with the peak magnitude at low wavenumbers ($k_z R = 1$) being smaller than at high wavenumber ($k_z R = 30$). Interestingly, $k_z E_{zz}/u_\tau^2$ at low wavenumbers are slightly smaller in the pipe than the channel. Figure 14(b) further shows the one dimensional pre-multiplied energy spectra $k_\theta E_{zz}/u_\tau^2$ at different y locations. Again, $k_\theta E_{zz}/u_\tau^2$ agrees well between the pipe and the channel at high wavenumbers. Consistent with those in the channel, a plateau appears for $5 \leq k_\theta \leq 30$ in the overlap region, with the magnitude increasing with y^+ . Such a plateau is present even in the viscous sublayer, which is the footprint of LSMs and VLSMs near the wall (Mathis *et al.* 2009; Hwang *et al.* 2016).

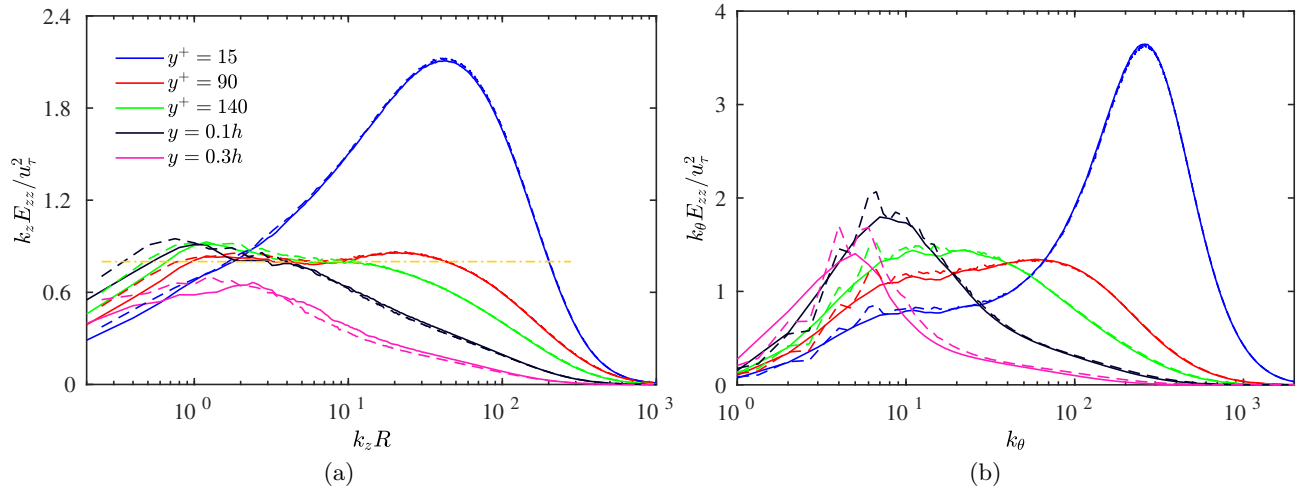


Figure 14: Comparison of the premultiplied energy spectra between pipe (solid) and channel (dashed) for $Re_\tau = 5200$: (a) $k_z E_{zz} / u_\tau^2$ and (b) $k_\theta E_{zz} / u_\tau^2$.

4. Concluding remarks

A new direct numerical simulation providing reliable high-fidelity data of turbulent pipe flow for Re_τ up to 5200 is presented. Particular focus has been put on providing data as accurate as possible; by using a high-order numerical method, large domains and sufficient integration time with quantified uncertainty. The DNS is performed with a pseudo-spectral code “OPENPIPEFLOW”, and the axial extent of the domain is $10\pi R$ (R is the pipe radius), which can be considered sufficiently long to capture all the relevant structures. A wealth of statistical data with uncertainty, including mean velocity, Reynolds stress and their budgets, pressure and its fluctuations, and energy spectra, is gathered (available online at <https://dataverse.tdl.org/dataverse/turbpipe>). An extensive comparison between our new pipe data and other simulation and experimental data is made, and small but still substantial and systematic differences between the various datasets are identified. For example, consistent lower values of the friction factor, wall shear stress fluctuations, and the inner peak of the axial velocity variance are observed for data generated using low order methods, such as Ahn *et al.* (2013) and Pirozzoli *et al.* (2021). In pipe flow simulation, the only parameter apart from the Re is the length of the pipe. Once the latter is chosen large enough, all data should, in principle, be the same. Such discrepancies between different simulations thus highlight the need for high-order accurate methods for this particular flow case. This argument is further complemented by performing an additional DNS at $Re_\tau = 2000$ with a spectral element code NEK5000, where all the statistical data generated are found to match well the results obtained using OPENPIPEFLOW.

Different from turbulent channel flow, the mean velocity has not yet developed a logarithmic region at $Re_\tau = 5200$, yet the diagnostic function collapses well between our $Re_\tau = 5200$ and the channel data of Lee & Moser (2015) and Hoyas *et al.* (2022) up to $y^+ \approx 250$ – suggesting a near-wall universality of the inner scaled mean velocity. The wall shear stress fluctuations, the inner peak of axial velocity variance, and the wall and peak of r.m.s. pressure fluctuations continuously increase with Re_τ , and their difference between pipe and channel decreases with increasing Re_τ . In addition, at the Re_τ range considered, the Re dependence of these quantities agrees with both the logarithmic and defect power scalings laws (Chen & Sreenivasan 2021). Consistent with observations in channel flow, one-dimensional spectra of the axial velocity exhibits a k^{-1} dependence at intermediate distances from the wall.

Acknowledgements. Computational and visualization resources provided by Texas Tech University HPCC, TACC Lonestar, Frontera, and Stampede2 under XSEDE are acknowledged. Parts of the computations were enabled by resources provided by the Swedish National Infrastructure for Computing (SNIC), partially funded by the Swedish Research Council through grant agreement no. 2018-05973. This work was partially supported by the National Science Foundation under award number (OAC-2031650) and President’s Endowed Distinguished Chair Funds. We wish to thank A. P. Willis for making the “openpipeflow” code open source, D. Massaro for help on the NEK5000 simulation, and X. Wu, P. Moin, C. Chin, S. Pirozzoli, M. Lee, L. Moser, and others for generously sharing their data.

| | | | | | |
|-------------------------------|------|------|------|------|------|
| Re_τ | 181 | 549 | 990 | 2001 | 5197 |
| Sampling interval (R/U_b) | 0.5 | 0.5 | 0.5 | 0.25 | 0.25 |
| Number of samples | 6228 | 1652 | 1301 | 1622 | 683 |

Table 4: Summary of the sampling of the flow variables used in the UQ analyses.

Declaration of interests. The authors report no conflict of interest

Data availability statement. The data that support the findings of this study are openly available from Texas Data Repository Dataverse at <https://dataverse.tdl.org/dataverse/turbpipe>.

Appendix A. Estimated uncertainties for one-point statistics

We briefly explain the approach employed to estimate the uncertainties in the mean velocity and Reynolds stress components of the DNS of the pipe flow. During the simulations, the time samples of the quantities contributing to statistical terms are averaged over the azimuthal (θ) and axial (z) directions. To compute the central statistical moments, the temporal correlation between the spatially-averaged quantities are preserved by, for instance, writing a Reynolds stress component as $\langle u'_r u'_z \rangle = \langle \bar{u}_r \bar{u}_z - \bar{u}_r \bar{u}_z \rangle$, where overbar means averaging over θ and z . In practice, the sample-mean estimator (SME) is used to estimate $\langle a \rangle$ from a finite number of time-series samples $\{a_i\}_{i=1}^n$, where $a_i = a(t_i)$ are equispaced time samples. The SME for $\langle a \rangle$ is defined as

$$\hat{\mu}_a := \hat{\mathbb{E}}[a] = \frac{1}{n} \sum_{i=1}^n a_i, \quad (\text{A } 1)$$

where $\hat{\mathbb{E}}[a]$ is the estimated expectation of a . Based on the central limit theorem (CLT), for a sufficiently large number of samples, the SME converges to the true expectation via a Gaussian distribution,

$$\hat{\mu}_a \sim \mathcal{N}(\mu_a, \sigma^2(\hat{\mu}_a)). \quad (\text{A } 2)$$

To estimate $\sigma(\hat{\mu}_a)$ and hence quantify the time-averaging uncertainty in $\hat{\mu}_a$, an analytical expression can be derived which depends on the autocorrelation of time-series a at different lags, see, e.g. [Oliver et al. \(2014\)](#); [Xavier et al. \(2022\)](#) and [Rezaeiravesh et al. \(2022\)](#). To avoid inaccuracy in $\sigma(\hat{\mu}_a)$ due to the oscillations in the sample-estimated autocorrelations, especially at higher lags, an autoregressive model is first fitted to the samples $\{a_i\}_{i=1}^n$ which is then used to construct a smooth model for the autocorrelations. The details of the approach can be found in [Oliver et al. \(2014\)](#) and [Xavier et al. \(2022\)](#). The main hyperparameters of this UQ approach are the order of the autoregressive model and the number of training lags when modeling the autocorrelation function (ACF). In the present study, the optimal values of these hyperparameters are chosen based on the sampling frequency of the data at each Re . All estimations of uncertainties have been performed using UQit ([Rezaeiravesh et al. 2021](#)).

Following the above approach, the uncertainty in the statistical moments of any order can be accurately estimated. However, there are various turbulence statistics that are defined as a combination of the exponents of various moments; for instance, consider the turbulence intensity, r.m.s. fluctuations, turbulent kinetic energy, various terms in the transport equations of the Reynolds stress components, etc. The uncertainty in such terms can be estimated by applying the approach described in [Rezaeiravesh et al. \(2022\)](#). The main idea for estimating the uncertainty in a compound statistical term is to estimate the uncertainty in its constitutive statistical moments and also estimate the cross-covariance between the SMEs corresponding to them. Following this procedure, in the DNS database reported online in connection with the present study, all statistics are accompanied by an accurate estimation of the corresponding time-averaging uncertainty. An important aspect of this procedure is that for the statistics expressed in wall units, the uncertainty of the wall friction velocity is also taken into account. This means, for instance, for $\langle u'_r u'_z \rangle^+$ the uncertainty of both $\langle u'_r u'_z \rangle$ and $\langle u_\tau \rangle^2$ are considered applying a Monte Carlo-based UQ forward problem, which does not require any linearization.

Table 4 summarizes the sampling interval and the total number of samples used for UQ for simulations

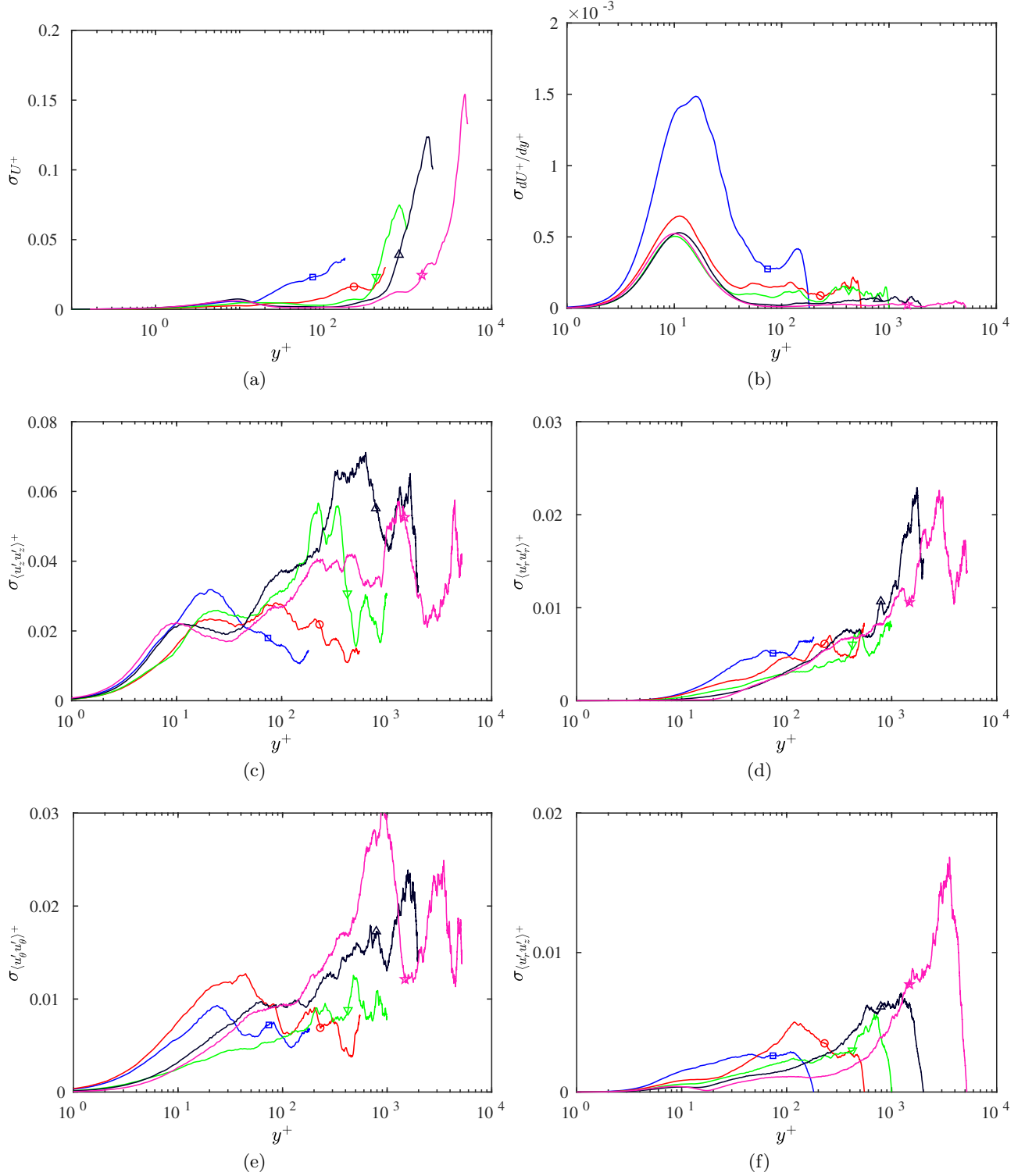


Figure 15: Estimated standard deviation of different statistical quantities: (a) U^+ ; (b) $\partial U^+ / \partial y^+$; (c) $\langle u_z'^2 \rangle^+$; (d) $\langle u_r'^2 \rangle^+$; (e) $\langle u_\theta'^2 \rangle^+$; (f) $\langle u_r' u_z' \rangle^+$.

at different Re_τ . Our investigation showed that for the collected samples, an autoregressive model of order 20 along with the sample-estimated ACF at the first 20 lags, for $Re_\tau = 180, 550, \text{ and } 1000$, and 40 lags, for $Re_\tau = 2000 \text{ and } 5200$, leads to accurate models for autocorrelation of various quantities. For low-order moments, using sample-estimated ACF at a higher number of lags, especially near the center of the pipe, could lead to slightly more accurate models for ACF. However, the difference in the resulting estimated uncertainty is below 1%.

Figure 15 shows the standard deviation σ , see (A 2), of the sample estimation of different inner-scaled statistical terms. Clearly, the estimated uncertainties vary between the moments and also in the wall-normal direction. However, for all quantities, the lowest uncertainty (corresponding to highest certainty) is observed near the wall. Moreover, the estimated uncertainty for each quantity exhibits a similar variation in the wall-normal direction for different Re_τ .

REFERENCES

- AFZAL, NOOR 1976 Millikan's argument at moderately large Reynolds number. *The Physics of Fluids* **19** (4), 600–602.
- AFZAL, NOOR 1982 Fully developed turbulent flow in a pipe: an intermediate layer. *Ingenieur-Archiv* **52** (6), 355–377.
- AFZAL, NOOR & YAJNIK, KIRIT 1973 Analysis of turbulent pipe and channel flows at moderately large Reynolds number. *Journal of Fluid Mechanics* **61** (1), 23–31.
- AHN, JUNSUN, LEE, JAE HWA, JANG, SUNG JAE & SUNG, HYUNG JIN 2013 Direct numerical simulations of fully developed turbulent pipe flows for $Re_\tau = 180, 544 \text{ and } 934$. *International journal of heat and fluid flow* **44**, 222–228.
- AHN, JUNSUN, LEE, JAE HWA, LEE, JIN, KANG, JI-HOON & SUNG, HYUNG JIN 2015 Direct numerical simulation of a 30R long turbulent pipe flow at $re_\tau = 3008$. *Physics of Fluids* **27** (6), 065110.
- ALFREDSSON, P HENRIK & ÖRLÜ, RAMIS 2010 The diagnostic plot—a litmus test for wall bounded turbulence data. *European Journal of Mechanics-B/Fluids* **29** (6), 403–406.
- BERNARDINI, MATTEO, PIROZZOLI, SERGIO & ORLANDI, PAOLO 2014 Velocity statistics in turbulent channel flow up to $Re_\tau = 4000$. *Journal of Fluid Mechanics* **742**, 171–191.
- BLASIUS, HEINRICH 1913 Das Ähnlichkeitsgesetz bei Reibungsvorgängen in Flüssigkeiten. In *Mitteilungen über Forschungsarbeiten auf dem Gebiete des Ingenieurwesens*, pp. 1–41. Springer.
- BUSCHMANN, MATTHIAS H & GAD-EL HAK, MOHAMED 2003 Generalized logarithmic law and its consequences. *AIAA journal* **41** (1), 40–48.
- CANTON, JACOPO, ÖRLÜ, RAMIS, CHIN, CHENG, HUTCHINS, NICHOLAS, MONTY, JASON & SCHLATTER, PHILIPP 2016 On large-scale friction control in turbulent wall flow in low Reynolds number channels. *Flow, Turbulence and Combustion* pp. 1–17.
- CANTWELL, BRIAN J 2019 A universal velocity profile for smooth wall pipe flow. *Journal of Fluid Mechanics* **878**, 834–874.
- CHEN, XI, HUSSAIN, FAZLE & SHE, ZHEN-SU 2019 Non-universal scaling transition of momentum cascade in wall turbulence. *Journal of Fluid Mechanics* **871**, R2.
- CHEN, XI & SREENIVASAN, KATEPALLI R 2021 Reynolds number scaling of the peak turbulence intensity in wall flows. *Journal of Fluid Mechanics* **908**.
- CHIN, C, MONTY, JP & OOI, A 2014 Reynolds number effects in dns of pipe flow and comparison with channels and boundary layers. *International journal of heat and fluid flow* **45**, 33–40.
- DEL ALAMO, JUAN C, JIMÉNEZ, JAVIER, ZANDONADE, PAULO & MOSER, ROBERT D 2004 Scaling of the energy spectra of turbulent channels. *Journal of Fluid Mechanics* **500**, 135–144.
- DOGAN, EDA, ÖRLÜ, RAMIS, GATTI, DAVIDE, VINUESA, RICARDO & SCHLATTER, PHILIPP 2018 Quantification of amplitude modulation in wall-bounded turbulence. *Fluid Dynamics Research* **51**, 011408.
- EGGELS, JGM, UNGER, F, WEISS, MH, WESTERWEEL, J, ADRIAN, RJ, FRIEDRICH, R & NIEUWSTADT, FTM 1994 Fully developed turbulent pipe flow: a comparison between direct numerical simulation and experiment. *Journal of Fluid Mechanics* **268**, 175–210.
- EL KHOURY, GEORGE K, SCHLATTER, PHILIPP, NOORANI, AZAD, FISCHER, PAUL F, BRETHOUWER, GEERT & JOHANSSON, ARNE V 2013 Direct numerical simulation of turbulent pipe flow at moderately high Reynolds numbers. *Flow, turbulence and combustion* **91** (3), 475–495.
- FELDMANN, DANIEL, BAUER, CHRISTIAN & WAGNER, CLAUS 2018 Computational domain length and Reynolds number effects on large-scale coherent motions in turbulent pipe flow. *Journal of Turbulence* **19** (3), 274–295.
- FIORINI, TOMMASO 2017 Turbulent pipe flow-high resolution measurements in ciclope. PhD thesis, alma.
- FURUICHI, N, TERAQ, Y, WADA, Y & TSUJI, Y 2015 Friction factor and mean velocity profile for pipe flow at high Reynolds numbers. *Physics of Fluids* **27** (9), 095108.
- FURUICHI, N, TERAQ, Y, WADA, Y & TSUJI, Y 2018 Further experiments for mean velocity profile of pipe flow at high Reynolds number. *Physics of Fluids* **30** (5), 055101.

- GUALA, M, HOMMEMA, SE & ADRIAN, RJ 2006 Large-scale and very-large-scale motions in turbulent pipe flow. *Journal of Fluid Mechanics* **554**, 521–542.
- HINZE, JO 1975 *Turbulence*. McGraw-Hill Publishing Co.
- HOYAS, SERGIO & JIMÉNEZ, JAVIER 2006 Scaling of the velocity fluctuations in turbulent channels up to $Re_\tau = 2003$. *Physics of fluids* **18** (1), 011702.
- HOYAS, SERGIO, OBERLACK, MARTIN, ALCÁNTARA-ÁVILA, FRANCISCO, KRAHEBERGER, STEFANIE V & LAUX, JONATHAN 2022 Wall turbulence at high friction Reynolds numbers. *Physical Review Fluids* **7** (1), 014602.
- HULTMARK, M., VALLIKIVI, M., BAILEY, S.C.C. & SMITS, A. J. 2012 Turbulent pipe flow at extreme Reynolds numbers. *Physics Review Letter* **108** (094501).
- HUSSAIN, AKMF & REYNOLDS, WC 1975 Measurements in fully developed turbulent channel flow. *Journal of Fluids Engineering* **97** (4), 568–578.
- HUTCHINS, N & MARUSIC, IVAN 2007 Evidence of very long meandering features in the logarithmic region of turbulent boundary layers. *Journal of Fluid Mechanics* **579**, 1–28.
- HWANG, JINYUL, LEE, JIN, SUNG, HYUNG JIN & ZAKI, TAMER A 2016 Inner–outer interactions of large-scale structures in turbulent channel flow. *Journal of Fluid Mechanics* **790**, 128–157.
- JIMÉNEZ, JAVIER 2012 Cascades in wall-bounded turbulence. *Annual Review of Fluid Mechanics* **44**, 27–45.
- JIMÉNEZ, JAVIER, HOYAS, SERGIO, SIMENS, MARK P & MIZUNO, YOSHINORI 2010 Turbulent boundary layers and channels at moderate Reynolds numbers. *Journal of Fluid Mechanics* **657**, 335–360.
- JIMÉNEZ, JAVIER & MOSER, ROBERT D 2007 What are we learning from simulating wall turbulence? *Philosophical Transactions of the Royal Society A: Mathematical, Physical and Engineering Sciences* **365** (1852), 715–732.
- KIM, JOHN 2011 Physics and control of wall turbulence for drag reduction. *Philosophical Transactions of the Royal Society of London A: Mathematical, Physical and Engineering Sciences* **369** (1940), 1396–1411.
- KIM, JOHN, MOIN, PARVIZ & MOSER, ROBERT 1987 Turbulence statistics in fully developed channel flow at low Reynolds number. *Journal of fluid mechanics* **177**, 133–166.
- KIM, KC & ADRIAN, RJ 1999 Very large-scale motion in the outer layer. *Physics of Fluids* **11** (2), 417–422.
- KLEWICKI, J.C. 2022 Bounded dissipation predicts finite asymptotic state of near-wall turbulence. *Journal of Fluid Mechanics* **940**, F1.
- LEE, JAE HWA & SUNG, HYUNG JIN 2013 Comparison of very-large-scale motions of turbulent pipe and boundary layer simulations. *Physics of Fluids* **25** (4), 045103.
- LEE, M. & MOSER, R. D. 2015 Direct numerical simulation of turbulent channel flow up to $Re_\tau = 5200$. *Journal of Fluid Mechanics* **774**, 395–415.
- LOZANO-DURÁN, ADRIÁN & JIMÉNEZ, JAVIER 2014 Effect of the computational domain on direct simulations of turbulent channels up to $re \tau = 4200$. *Physics of Fluids* **26** (1), 011702.
- LUCHINI, PAOLO 2017 Universality of the turbulent velocity profile. *Physical review letters* **118** (22), 224501.
- MARUSIC, I., BAARS, W.J. & HUTCHINS, N. 2017 Scaling of the streamwise turbulence intensity in the context of inner-outer interactions in wall turbulence. *Physical Review Fluids* **2** (100502).
- MARUSIC, I, MATHIS, R & HUTCHINS, N 2010a Predictive model for wall-bounded turbulent flow. *Science* **329** (5988), 193–196.
- MARUSIC, I., MCKEON, B. J., MONKEWITZ, P. A., NAGIB, H. M., SMITS, A. J. & SREENIVASAN, K. R. 2010b Wall-bounded turbulent flows at high Reynolds numbers: Recent advances and key issues. *Phys. Fluids* **22** (6), 065103.
- MARUSIC, IVAN & MONTY, JASON P 2019 Attached eddy model of wall turbulence. *Annual Review of Fluid Mechanics* **51**, 49–74.
- MARUSIC, IVAN, MONTY, JASON P, HULTMARK, MARCUS & SMITS, ALEXANDER J 2013 On the logarithmic region in wall turbulence. *Journal of Fluid Mechanics* **716**, R3.
- MATHIS, ROMAIN, HUTCHINS, NICHOLAS & MARUSIC, IVAN 2009 Large-scale amplitude modulation of the small-scale structures in turbulent boundary layers. *Journal of Fluid Mechanics* **628**, 311–337.
- MCKEON, BJ, ZAGAROLA, MV & SMITS, AJ 2005 A new friction factor relationship for fully developed pipe flow. *Journal of fluid mechanics* **538**, 429–443.
- MONTY, JP, HUTCHINS, N, NG, HCH, MARUSIC, I & CHONG, MS 2009 A comparison of turbulent pipe, channel and boundary layer flows. *Journal of Fluid Mechanics* **632**, 431–442.
- MONTY, JP, STEWART, JA, WILLIAMS, RC & CHONG, MS 2007 Large-scale features in turbulent pipe and channel flows. *Journal of Fluid Mechanics* **589**, 147–156.
- MOSER, ROBERT D, KIM, JOHN & MANSOUR, NAGI N 1999 Direct numerical simulation of turbulent channel flow up to $Re_\tau = 590$. *Physics of fluids* **11** (4), 943–945.
- NAGIB, HASSAN M & CHAUHAN, KAPIL A 2008 Variations of von kármán coefficient in canonical flows. *Physics of Fluids* **20** (10), 101518.
- NICKELS, TB, MARUSIC, I, HAFEZ, S & CHONG, MS 2005 Evidence of the k^{-1} law in a high-Reynolds-number turbulent boundary layer. *Physical Review Letters* **95** (7), 074501.
- NIKURADSE, JOHANN 1933 Strömungsgesetze in rauhen Röhren. *VDI Forschungsheft* **361**, 1.
- OLIVER, TODD A., MALAYA, NICHOLAS, ULERICH, RHYS & MOSER, ROBERT D. 2014 Estimating uncertainties

- in statistics computed from direct numerical simulation. *Physics of Fluids* **26** (3), 035101, arXiv: <https://doi.org/10.1063/1.4866813>.
- ÖRLÜ, RAMIS & SCHLATTER, PHILIPP 2011 On the fluctuating wall-shear stress in zero pressure-gradient turbulent boundary layer flows. *Physics of fluids* **23** (2), 021704.
- PERRY, AE, HENBEST, S & CHONG, MS0597 1986 A theoretical and experimental study of wall turbulence. *Journal of Fluid Mechanics* **165**, 163–199.
- PIROZZOLI, SERGIO, ROMERO, JOSHUA, FATICA, MASSIMILIANO, VERZICCO, ROBERTO & ORLANDI, PAOLO 2021 One-point statistics for turbulent pipe flow up to $Re_\tau \approx 6000$. *Journal of Fluid Mechanics* **926**, A28.
- POPE, S. B. 2000 *Turbulent flows*. Cambridge university press.
- REZAEIRAVESH, SALEH, VINUESA, RICARDO & SCHLATTER, PHILIPP 2021 UQit: A Python package for uncertainty quantification (UQ) in computational fluid dynamics (CFD). *Journal of Open Source Software* **6** (60), 2871.
- REZAEIRAVESH, SALEH, YAO, JIE, HUSSAIN, FAZLE & SCHLATTER, PHILIPP 2022 Recipes for quantifying time-averaging uncertainties in turbulence statistics. *To be submitted* .
- ROSENBERG, BJ, HULTMARK, MARCUS, VALLIKIVI, MARGIT, BAILEY, SEAN CHRISTOPHER COLLISON & SMITS, ALEXANDER J 2013 Turbulence spectra in smooth-and rough-wall pipe flow at extreme Reynolds numbers. *Journal of Fluid Mechanics* **731**, 46–63.
- SCHLATTER, PHILIPP & ÖRLÜ, RAMIS 2010 Assessment of direct numerical simulation data of turbulent boundary layers. *Journal of Fluid Mechanics* **659**, 116–126.
- SCHOPPA, W. & HUSSAIN, F. 2002 Coherent structure generation in near-wall turbulence. *Journal of fluid Mechanics* **453**, 57–108.
- SHE, ZHEN-SU, CHEN, XI & HUSSAIN, FAZLE 2017 Quantifying wall turbulence via a symmetry approach: a lie group theory. *Journal of Fluid Mechanics* **827**, 322–356.
- SILLERO, JUAN A, JIMÉNEZ, JAVIER & MOSER, ROBERT D 2013 One-point statistics for turbulent wall-bounded flows at reynolds numbers up to $\delta^+ \approx 2000$. *Physics of Fluids* **25** (10), 105102.
- SMITS, AJ, MONTY, J, HULTMARK, MARCUS, BAILEY, SEAN CHRISTOPHER COLLISON, HUTCHINS, NICHOLAS & MARUSIC, IVAN 2011a Spatial resolution correction for wall-bounded turbulence measurements. *Journal of Fluid Mechanics* **676**, 41–53.
- SMITS, ALEXANDER J, HULTMARK, MARCUS, LEE, MYOUNGKYU, PIROZZOLI, SERGIO & WU, XIAOHUA 2021 Reynolds stress scaling in the near-wall region of wall-bounded flows. *Journal of Fluid Mechanics* **926**.
- SMITS, ALEXANDER J, MCKEON, BEVERLEY J & MARUSIC, IVAN 2011b High-reynolds number wall turbulence. *Annual Review of Fluid Mechanics* **43**.
- SREENIVASAN, KR 1989 The turbulent boundary layer. In *Frontiers in experimental fluid mechanics*, pp. 159–209. Springer.
- TALAMELLI, ALESSANDRO, PERSIANI, FRANCO, FRANSSON, JENS HM, ALFREDSSON, P HENRIK, JOHANSSON, ARNE V, NAGIB, HASSAN M, RÜEDI, JEAN-DANIEL, SREENIVASAN, KATEPALLI R & MONKEWITZ, PETER A 2009 CICLOPE—a response to the need for high Reynolds number experiments. *Fluid Dynamics Research* **41** (2), 021407.
- WALEFFE, FABIAN 1997 On a self-sustaining process in shear flows. *Physics of Fluids* **9** (4), 883–900.
- WILLERT, CHRISTIAN E, SORIA, JULIO, STANISLAS, MICHEL, KLINNER, JOACHIM, AMILI, Omid, EISFELDER, MICHAEL, CUVIER, CHRISTOPHE, BELLANI, GABRIELE, FIORINI, TOMMASO & TALAMELLI, ALESSANDRO 2017 Near-wall statistics of a turbulent pipe flow at shear Reynolds numbers up to 40 000. *Journal of Fluid Mechanics* **826**, R5.
- WILLIS, A. P. 2017 The Openpipeflow Navier–Stokes solver. *SoftwareX* **6**, 124–127.
- WU, XIAOHUA, BALTZER, JR & ADRIAN, RJ 2012 Direct numerical simulation of a 30R long turbulent pipe flow at $R^+ = 685$: large-and very large-scale motions. *Journal of Fluid Mechanics* **698**, 235–281.
- WU, XIAOHUA & MOIN, PARVIZ 2008 A direct numerical simulation study on the mean velocity characteristics in turbulent pipe flow. *Journal of Fluid Mechanics* **608**, 81–112.
- XAVIER, DONNATELLA, REZAEIRAVESH, SALEH, VINUESA, RICARDO & SCHLATTER, PHILIPP 2022 Reliable quantification of time-averaging uncertainties in turbulent flow simulations. *To be submitted* .
- YANG, XIANG IA, HONG, JIARONG, LEE, MYOUNGKYU & HUANG, XINYI LD 2021 Grid resolution requirement for resolving rare and high intensity wall-shear stress events in direct numerical simulations. *Physical Review Fluids* **6** (5), 054603.
- YANG, XIYANG IA & LOZANO-DURÁN, ADRIÁN 2017 A multifractal model for the momentum transfer process in wall-bounded flows. *Journal of fluid mechanics* **824**.
- YAO, JIE, CHEN, XI & HUSSAIN, FAZLE 2018 Drag control in wall-bounded turbulent flows via spanwise opposed wall-jet forcing. *Journal of Fluid Mechanics* **852**, 678–709.
- ZAGAROLA, M. V. & SMITS, A. J. 1998 Mean-flow scaling of turbulent pipe flow. *J. Fluid Mech.* **373**, 33–79.